Vol. 02 No. 02 2024

RiESTech

JOURNAL RECENT IN ENGINEERING SCIENCE AND TECHNOLOGY

MBI

E- ISSN : 2985-8321
P -ISSN : 2985-704X

Recent in Engineering Science and Technology (RiESTech)
PT MENCERDASKAN BANGSA INDONESIA (MBI)
Available online at: http://www.mbi-journals.com/index.php/riestech

E- ISSN : 2985-8321
P -ISSN : 2985-704X

Recent in Engineering Science and Technology (RiESTech)

Volume 2 No 2 April 2024

FOCUS AND SCOPE

RIESTECH

Recent in Engineering Science and Technology **(RiESTech):** I*SSN: 2985-704X (print), ISSN: 2985-8321 (online)* a peer-reviewed quarterly engineering journal, publishes theoretical and experimental high-quality papers to promote engineering and technology's theory and practice. In addition to peer-reviewed original research papers, the Editorial Board welcomes original research reports, state-of-the-art reviews, and communications in the broadly defined field of recent engineering science and technology. **RiESTech** covers topics contributing to a better understanding of engineering, material science, computer science, environmental science, and their applications. **RiESTech** is concerned with scientific research on mechanical and civil engineering, Electrical/Electronics and Computer Engineering, and Metallurgical and Materials Engineering with specific analytical techniques and/or computational methods.

The frequency of RiESTech publications is four times a year namely in January, April, July, and October. The scope of RiESTech includes a wide spectrum of subjects namely:

Mechanical and Civil Engineering (Automotive Technologies; Construction Materials; Design and Manufacturing; Dynamics and Control; Energy Generation, Utilization, Conversion, and Storage; Fluid Mechanics and Hydraulics; Heat and Mass Transfer; Micro-Nano Sciences; Renewable and Sustainable Energy Technologies; Robotics and Mechatronics; Solid Mechanics and Structure; Thermal Sciences)

Electrical/Electronics and Computer Engineering (Instrumentation; Coding, Cryptography, and Information Protection; Communications, Networks, Mobile Computing, and Distributed Systems; Compilers and Operating Systems; Parallel Processing, and Dependability; Computer Vision and Robotics; Control Theory; Electromagnetic Waves, Microwave Techniques and Antennas; Embedded Systems; Integrated Circuits, VLSI Design, Testing, and CAD; Microelectromechanical Systems; Microelectronics, and Electronic Devices and Circuits; Power, Energy and Energy Conversion Systems; Signal, Image, and Speech Processing; Machine Learning and Data Science)

E- ISSN : 2985-8321
P -ISSN : 2985-704X

Metallurgical and Materials Engineering (Advanced Materials Science; Ceramic and Inorganic Materials; Electronic-Magnetic Materials; Energy and Environment; Materials Characterization; Metallurgy Extractive; Polymers and Nanocomposites)

Environmental Science and Engineering (Waste Management, Climate Change, Zero Waste, Environmental Disaster Management, Circular Economy, Sustainable Development, Environmental Security, Environmental Management, Environmental Ecology, Conservation of Natural Resources And Environment, Environmental Impact Analysis, Planning and Environmental Administration, Environmental Health, Environmental Pollution, Environmental Accounting, and Environmental Information Systems)

Recent in Engineering Science and Technology (RiESTech)
PT MENCERDASKAN BANGSA INDONESIA (MBI)
Available online at: http://www.mbi-journals.com/index.php/riestech

E- ISSN : 2985-8321
P -ISSN : 2985-704X

Recent in Engineering Science and Technology

(RiESTech)

Volume 2 No 2 April 2024

E- ISSN : 2985-8321
P -ISSN : 2985-704X

Layout and Typesetting:

Imam Sapto Nugroho, Universitas Indonesia (Alumni), Indonesia
Kamil Raihan Permana, Universitas Indonesia, Indonesia
Raihan Trinanda Agsya, Politeknik Negeri Jakarta, Indonesia

PUBLISHER
PT MENCERDASKAN BANGSA INDONESIA (MBI)
Address : 4th Floor Gedung STC Senayan Room 31-34, Jl. Asia Afrika Pintu IX, Jakarta 10270, Indonesia.

Recent in Engineering Science and Technology (RiESTech)
PT MENCERDASKAN BANGSA INDONESIA (MBI)
Available online at: http://www.mbi-journals.com/index.php/riestech

E- ISSN : 2985-8321
P -ISSN : 2985-704X

Recent in Engineering Science and Technology (RiESTech)

Volume 2 No 2 April 2024

PREFACE

Journal RiESTech (p-ISSN: 2985-704X (print), e-ISSN: 2985-8321 (online); is a peer review journal published by PT Mencerdaskan Bangsa Indonesia. The RiESTech journal is published four times a year in January, April, July, and October. This journal provides direct open access to its content on the principle that making research freely available to the public supports a greater global exchange of knowledge within the engineering field. This journal aims to provide a place for academics, researchers, and practitioners to publish original research articles or review articles. The scope of articles published in this journal relates to various topics in the field of outcomes of research activities.

The RiESTech journal publishes papers strictly following the RiESTech guidelines and templates for manuscript preparation. All submitted manuscripts will go through a double-blind peer review process. The paper is read by members of the editor (according to the area of specialization) and will be screened by the Managing Editor to meet the criteria required for RiESTech publication. Manuscripts will be sent to two reviewers based on their historical experience in reviewing manuscripts or based on their areas of specialization. RiESTech has review forms to keep the same item reviewed by two reviewers. Then the editorial board makes a decision on the comments or suggestions of the reviewers.

Reviewers provide an assessment of originality, clarity of presentation, contribution to the field/science. This journal publishes research articles, review articles/literature reviews, case reports and concept/policy articles, in all fields of Computer Science, Informatics Engineering, Multimedia, Arts. The article to be published is an original work and has never been published. Incoming articles will be reviewed by the reviewer team.

The Editorial Board will try to continue to improve the quality of the journal so that it can become an important reference in the development of engineering sciences. The greatest appreciation and gratitude to Mitra Bestari along with members of the Editorial Board and all parties involved in the publication of this journal. Complete writing instructions are displayed on the portal of this journal.

Regards,

Chief Editor

Recent in Engineering Science and Technology (RiESTech)
PT MENCERDASKAN BANGSA INDONESIA (MBI)
Available online at: http://www.mbi-journals.com/index.php/riestech

E- ISSN : 2985-8321
P -ISSN : 2985-704X

Recent in Engineering Science and Technology (RiESTech)

Volume 2 No 2 April 2024

Contents

Articles

RiESTech
Recent in Engineering Science and Technology

MBI

Article

Analysis of the Effect of Feeder Volume on Shrinkage Porosity Defects in Piston Products through the Gravity Die Casting Process

Nabila Banowati [1], Muhammad Fernanda Alvi Yasin [1], Veronika Noviaty [1], Sugeng Mulyono [1], Tia Rahmiati [1], Wandi Wahyudi [2], Vika Rizkia [1,*]

[1] Mechanical Engineering, Politeknik Negeri Jakarta, Jl. Prof.G.A Siwabessy, Kampus UI, Depok, 16425, Indonesia
[2] Physical Sciences and Engineering (PSE), King Abdullah University of Science and Technology (KAUST), Saudi Arabia 23955
* Correspondence: vika.rizkia@mesin.pnj.ac.id

Abstract: To achieve defect-free casting (soundness casting) with a minimal amount of shrinkage porosity, refinement during the casting process is necessary. In the gravity die casting process, there are parameters that lead to product defects, especially in the casting design, focusing on the gating system and feeder system as pathways for the flow of molten metal to supply the molten metal into the mold cavity. This research was conducted to examine the effect of adding feeder dimensions on shrinkage porosity, specifically on Al-Si piston products with a Silicon content of 12-13%. Feeder dimensions were varied in nine variations by adding height and width to the feeder gate, initially measuring 90mm in height and 32mm in width, along with the addition of insulation to the feeder to retain the heat of the casting process. Cooling used water and argon, with water placed at the center core and pin core and argon placed on the outer mold, with a solidification time of 150 seconds and pouring time of 3 seconds considered constant. This study used a Computer Aided Engineering (CAE) approach, namely MagmaSoft or the application of software to model the gravity casting system process. The results showed the lowest percentage of shrinkage at feeder dimensions of 114mm in height and 45mm in width with a mold temperature of 220°C was 0.76% of the product.

Keywords: Gravity Die Casting; Feeder; Piston; Shrinkage Porosity; Magmasoft Analysis

Citation:. Banowati, N., Yasin, M. F. A., Noviaty, V., Mulyono, S., Rahmiati, T., Wahyudi, W., Rizkia, V. (2024). Analysis of the Effect of Feeder Volume on Shrinkage Porosity Defects in Piston Products through the Gravity Die Casting Process. Recent in Engineering Science and Technology, 2(02), 1–17. Retrieved from https://www.mbi-journals.com/index.php/riestech/article/view/56

Academic Editor: Iwan Susanto

Received: 26 April 2024
Accepted: 29 April 2024
Published: 30 April 2024

Publisher's Note: MBI stays neutral with regard to jurisdictional claims in published maps and institutional affiliations.

1. Introduction

The time-varying temperature profiles significantly impact the occurrence of shrinkage porosity defects in castings during the solidification process. The temperature gradients inside the component dictate whether a location in the process of solidification has adequate access to a higher-temperature feed metal[1,2]. Shrinkage porosity will form in areas where volume decreases as a result of phase shift without any access to the main metal supply. These regions are commonly referred to as "hot spots" due to the presence of islands of hot metal surrounded by colder material[3–5]. The current study focused on a shrinkage porosity problem that one of the automotive companies was trying to fix in their aluminum foundry, as depicted in Figure 1. Shrinkage porosity was present in the crown section, the center of the pin boss, and the pin center of the piston product, which is located near the feed system. According to reports, 90 percent of shrinkage problems occur as a result of inadequate casting design[6–9], which in turn impacts the process of filling the mold and subsequently impacts the mechanical properties of the cast material[10–12].

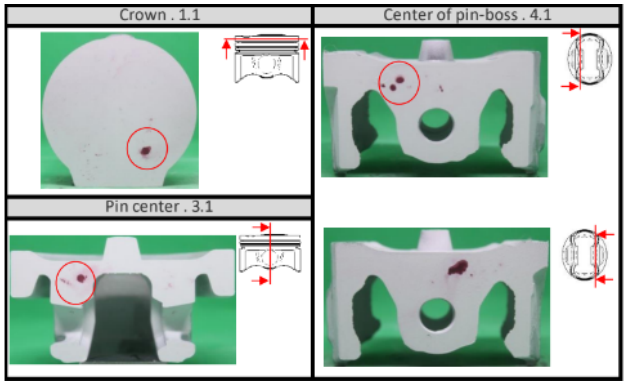

Figure 1. A cross-section of an aluminum alloy piston. The red circles indicate casting walls containing the shrinkage porosity.

The study aimed to discover the effect of feeder dimension and die temperature on shrinkage porosity and determine effective measures to mitigate this defect, ensuring that the parts successfully passed a leak test. Due to the heavy production program, physical experimentation on the manufacturing line was impossible. Therefore, software simulations of the process were suggested instead. In numerous sectors of the industry at present, software simulations are progressively replacing physical experiments[13–16]. Numerical experiments are conducted to determine the optimal process parameters and tooling to ensure that products are manufactured accurately from the first time, thereby avoiding costly and time-consuming physical experimentation. Furthermore, to address casting defects, researchers have developed mathematical models, which were integrated into simulation software[17–21]. MAGMAsoft, renowned for its capabilities in simulating and optimizing casting processes, was utilized for conducting numerical simulations. These numerical simulations were utilized to detect problems virtually. The use of virtual simulations offers several advantages to manufacturers, including improved quality and reduced production costs[22–24].

Gunasegaram et al. utilized numerical simulation and experimental design to establish the key factors that affect the shrinkage porosity in permanent mold castings, aiming to attain an optimal outcome. It was found that the presence of a thick layer of mold, along with a high temperature of the mold, caused a large displacement of shrinkage porosity from critical areas [5]. Dabade et al. utilized the design of experiments and the Taguchi approach to determine the primary process parameter that affects the casting process. To mitigate shrinkage porosity in the cast component, a solidification study was conducted utilizing computer simulation software using innovative gating and feeding methods. Their findings revealed a notable reduction in shrinkage porosity and an enhancement in casting yield [24]. The use of computer simulations to identify casting defects that form during the solidification phase of casting components was investigated by Vijayaram et al. They provided evidence that these simulations benefited the foundry industry significantly[25].

In this study, numerical simulation techniques were utilized to reduce the occurrence of shrinkage porosity defects in the gravity die-casting process. MAGMAsoft was utilized to simulate the cast component in a realistic manner, and the simulation results were integrated into real-time casting. The effect of feeder dimension and die temperature on shrinkage porosity in piston products of one of the automotive companies has become a novelty.

2. Materials and Experiment Methods

This work uses the Magma5 Version 5.3.0 software platform to model the complete casting process. The CAE simulation procedure is executed according to this methodology. CAD software is utilized to create an accurate geometrical model of the gravity die-casting system based on actual dimensions. Pre-processing is the initial stage of analyzing

a computational model. This stage consists of creating boundary conditions and meshing, defining the materials used or determining the domain, defining related parameters, and creating geometry. After that, cavity filling simulation is conducted using the specimen of AC8A (AlSi12CuNiMg) with the pouring and die temperatures of 740°C and 220°C, respectively. In this study, the original design as seen in Table 1. was altered to reduce the occurrence of shrinkage porosity defects in the cast product. This was achieved by modifying the feeder height to 98, 106.5, and 115 mm, and adjusting the feeder gate to 40, 44, and 48 mm. Moreover, post-processing is done after cavity filling simulation in order to simulate the casting process during the solidification stage, including fraction solid solidification, temperature distribution, potential hot spot locations that may result in casting defects, and shrinkage porosity. Once the casting simulation utilizing the CAD technique yields optimal results, the validation is performed by manual gravity die casting as seen in Figure 2. The quality check of validation cast products is done by dye penetrant test and microstructure analysis.

Table 1. Gating system parameters of the initial design

Piston weight (1 cavity)	233.2 gr
Piston volume	84985 mm^3
Feeder height	82 mm
Feeder gate	32 mm

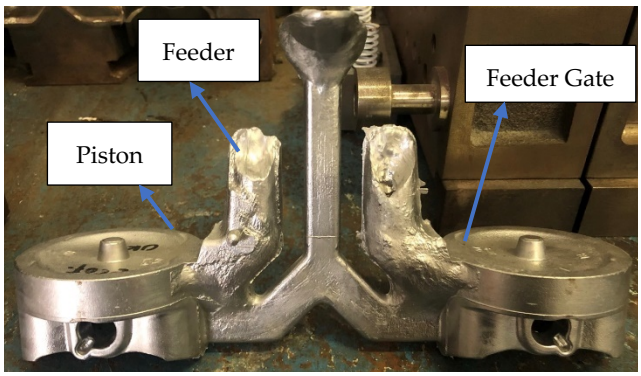

Figure 2. Blank Casting of the Piston

3. Results and Discussion

3.1. Analysis of The Initial Design

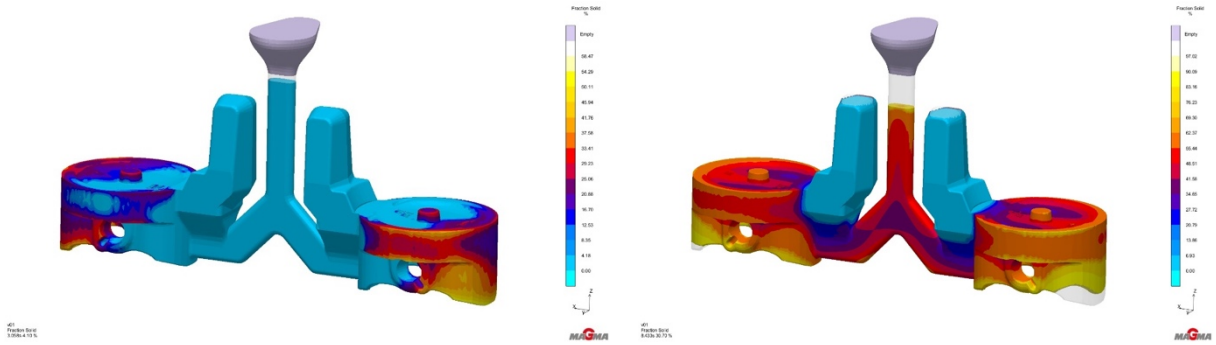

(a) (b)

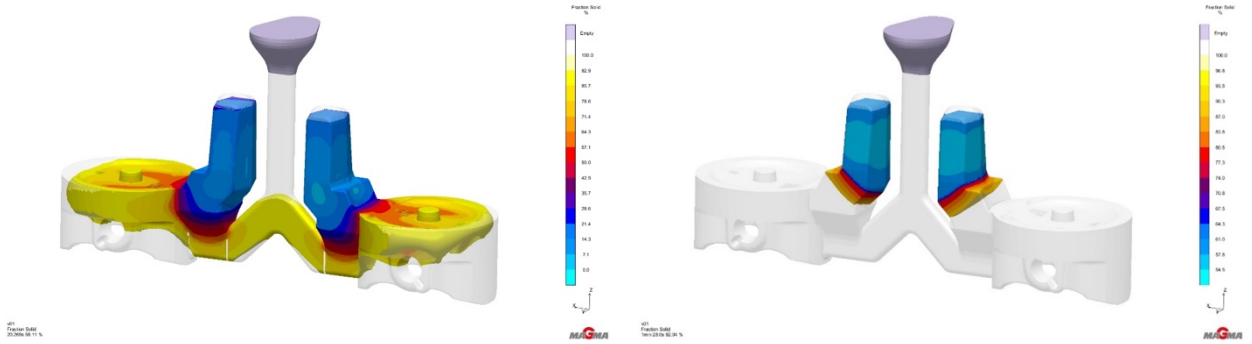

(c) (d)

Figure 3. The phase transition from liquid to solid during solidification at (a) 3.058 s (b) 8.433 s (c) 20.269 s (d) 88s on piston product using initial design

Figure 3. illustrates the phase transition process from liquid to solid. The blue-colored section shows the condition where the molten metal begins to fill the mold cavity, while the sections other than blue indicate the product undergoes solidification. At 3.058 seconds, the product initiates solidification in the outermost region as a result of direct contact with the mold. Solidification continues until approximately 8.433 seconds; at this point, the product turns into a mud phase with 40-70% solid formation, as illustrated in Figure 3(b). At 20.269 seconds (Figure 3(c)), the product solidifies with a solid formation of about 60% to 90%. Moreover, it is noted that the liquid undergoes a transition to become a solid. However, the thickest part adjacent to the feeder gate still exhibits an orange color, indicating that it remains in a liquid metal form. The greater thickness part signifies a deceleration in the solidification process, which may result in shrinkage formation. Upon reaching complete solidification, the final stage of solidification occurs in the gating system, particularly in the feeder section. At 88 seconds, the feeder continues to solidify, allowing it to withdraw any liquid metal from the piston product that has not completely solidified yet, as illustrated in Figure 3(d).

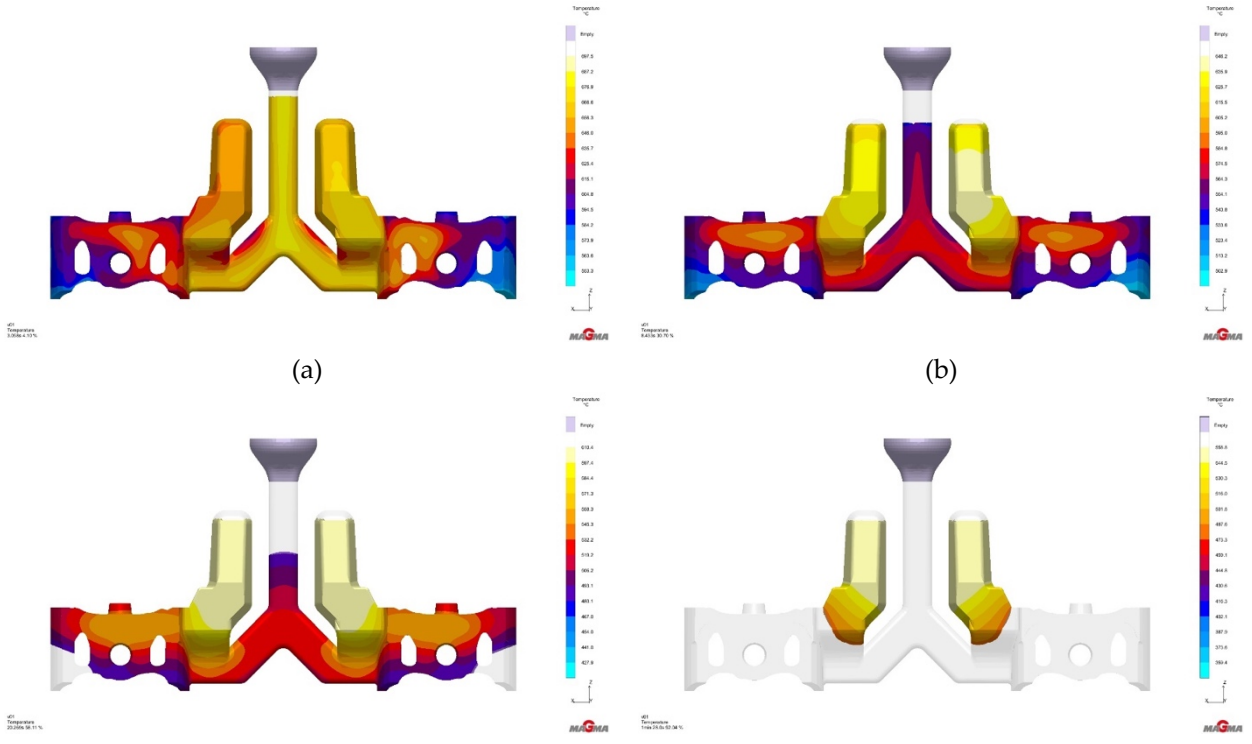

(a) (b)

(c) (d)

Figure 4. Temperature changes during the solidification process at (a) 3.058 s (b) 8.433 s (c) 20.269 s (d) 88s on piston product using initial design

Figure 4. depicts the temperature gradient that occurs during the solidification process. The blue color indicates a temperature decrease as the high-temperature molten metal comes into contact with the mold at 220°C, initiating the transition from liquid to solid. As shown in Figure 4 (a), the molten metal's temperature decreases when it comes into contact with the mold at an initial pouring temperature of 740°C. At 3.058 seconds, the highest temperatures reach 660.7°C and 658.5°C, whereas the temperatures of the solidified cast are 603.9°C and 607.9°C. This temperature difference can cause shrinkage, as depicted in Figures 4(b) and (c). The highest temperatures, reaching 598.7°C and 552.7°C, are found in the thickest part near the pinhole. The part that solidifies faster is the thinnest section of the product. Once this part has solidified, the molten metal cannot fill the voids in the surrounding area. Based on Figure 4, the simulation results have shown uneven temperature distribution during the solidification process, leading to hot spot formation where shrinkage takes place. Therefore, geometric changes are necessary in the feeder system to maximize the supply of molten metal to the product during early solidification stages.

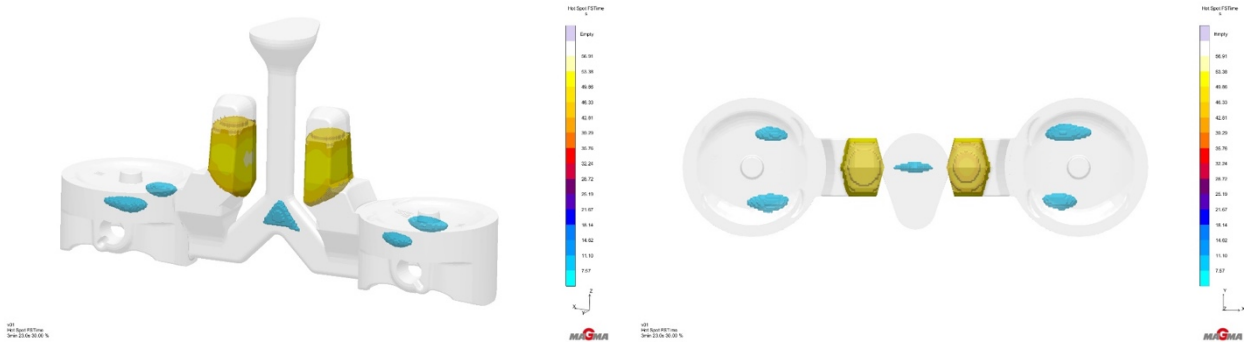

(a) (b)

Figure 5. The critical points where defects are likely to occur

Hot spots indicate the solidification time at the peak area from the liquidus to the temperature where there is no longer a supply flow from the feeder system. As a result, they represent the highest temperature implemented from the effectiveness value of the supply stored in the alloy material dataset, depicting the solidified molten parts and the potential for defects. Figure 5(a) and (b) display the front view and the top view, respectively, of the critical points (hot spots) corresponding to the hottest temperature when the product reaches 100% solid condition.

There is a potential for shrinkage porosity defects evident from the location of critical points (Hot Spots) on the crown, center of pin-boss, and pin center near the feeder system, as shown in Figure 1. The image confirms that the porosities formed during the final stages of solidification with the product at 100% solid condition align with their critical point locations due to temperature discrepancies during the solidification process. These areas experience slower solidification compared to thinner sections, resulting in insufficient material supply from the feeder system. The shrinkage porosity magnitude formed from 2 cavities amounts to 11.33%. Generally, it is advantageous that approximately 90% of the shrinkage occurs in the feeder rather than in the product. To address this issue, adjustments in feeder height, feeder gate width, and the addition of insulation to the feeder system are necessary to retain heat from the casting process and prevent gas bubble formation due to the molten metal's heat. Additionally, monitoring mold temperatures is crucial to guide solidification effectively.

3.2. Analysis of Modification Design

In order to address shrinkage porosity defects, modifications are made to the feeder dimensions as seen in Table 2. In this study, adjustments will be made to increase the height and width of the feeder gate, as well as the addition of insulation to retain heat during the casting process.

Table 2. Design variation in feeder system dimension

Design	Feeder height (mm)	Feedergate width (mm)
1	98	40
2	98	44
3	98	48
4	106.5	40
5	106.5	44
6	106.5	48
7	115	40
8	115	44
9	115	48

The solidification rate significantly influences the strength and hardness of the product. The casting process for this type of piston typically requires a solidification time of around 150 seconds based on field trials with favorable outcomes. Total solidification time refers to the duration of the molten metal being poured until the mold is opened again in the gravity casting process. In this research, the Magma software provides information about the optimal solidification flow of the product in percentage at specific temperatures. Figure 6. depicts comparisons of the transition from liquid to solid for each variation.

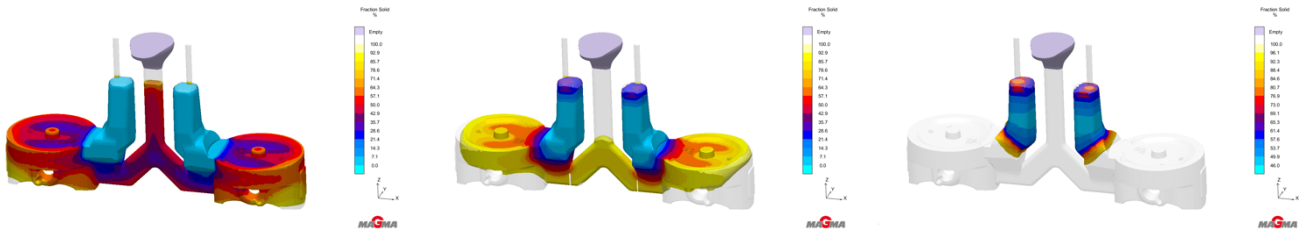

(a)

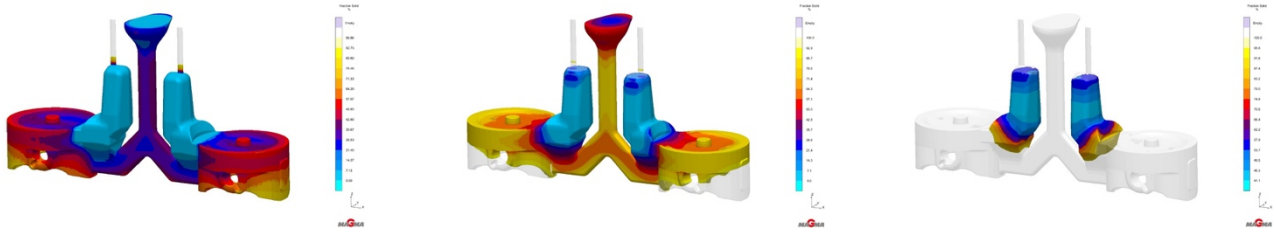

(b)

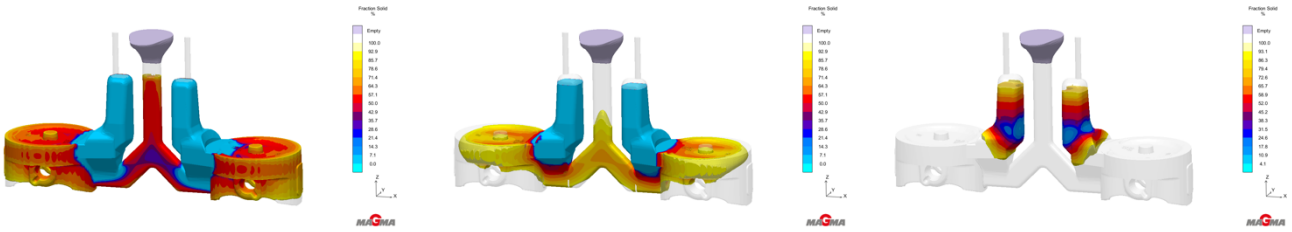

(c)

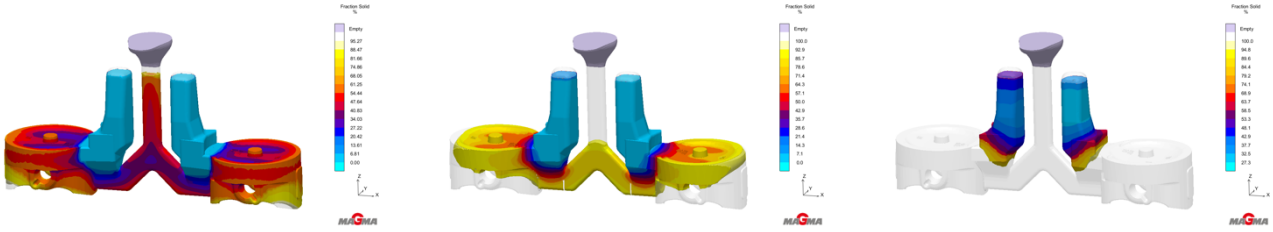

(d)

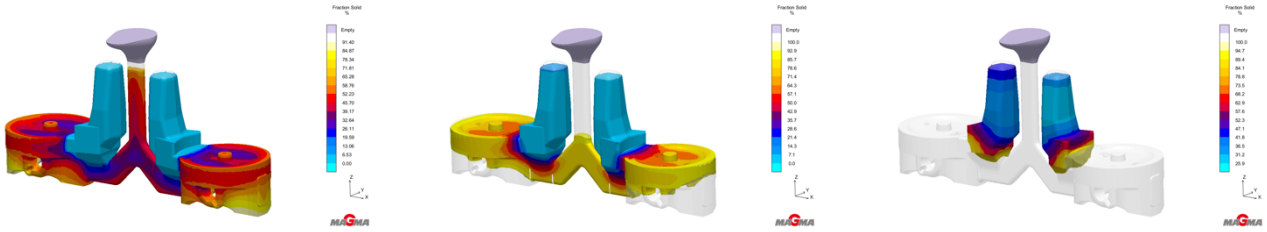

(e)

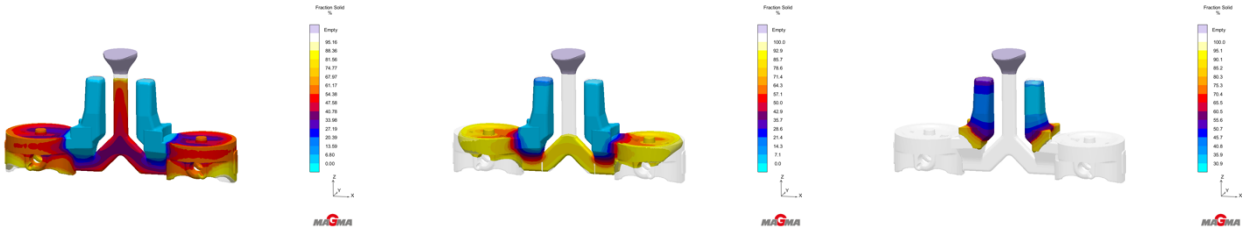

(f)

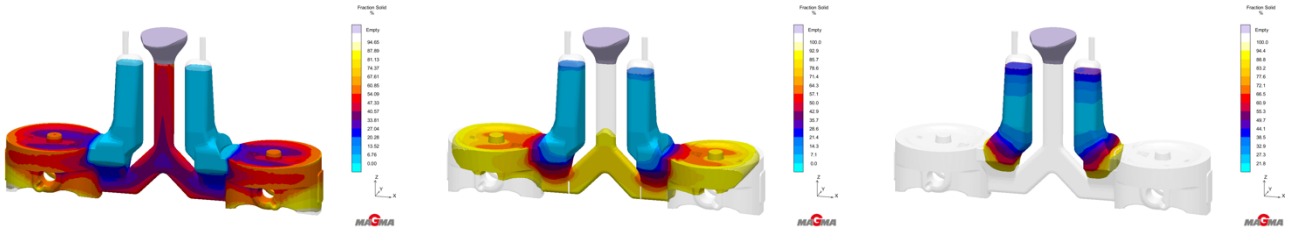

(g)

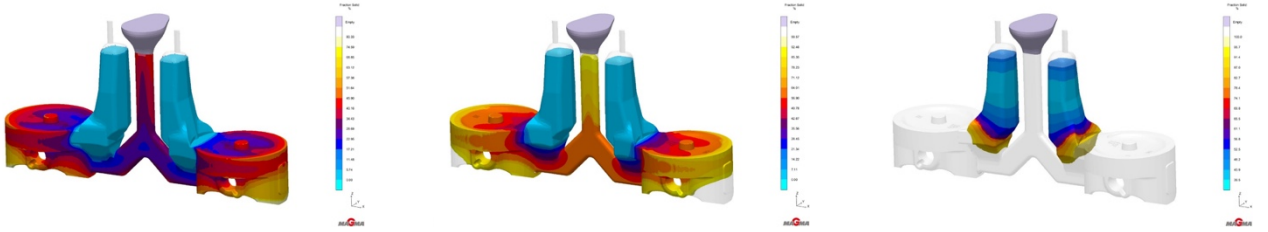

(h)

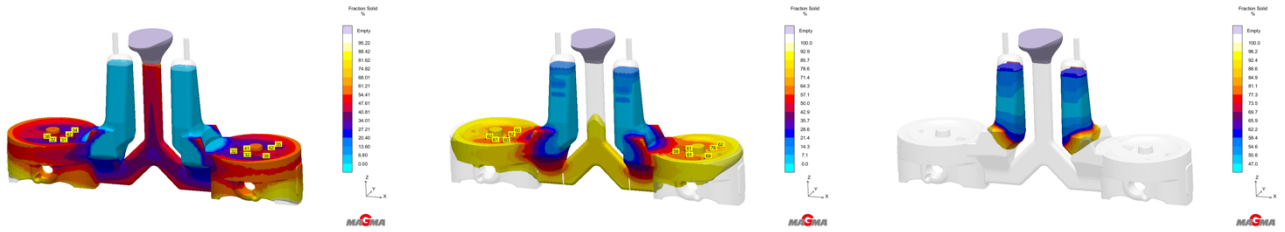

(i)

Figure 6. Solid fraction of all designs (a) 1st variation, (b) 2nd variation (c) 3rd variation (d) 4th variation (e) 5th variation, (f) 6th variation, (g) 7th variation, (h) 8th variation, (i) 9th variation, observed at time intervals of 8.433 s, 20.269 s, and 88 s from left to right.

As depicted in Figure 6, the solidification process simulation is represented in percentage (%) at specific periods. The uniformity of the solidification process is denoted by the colors of blue, yellow, red, and orange. Blue indicates that the product is still in the liquid phase; yellow implies complete solidification; and red and orange signify the product is in the mud phase, meaning that the phase transition from liquid to solid is not yet complete. Although no substantial changes are observed among the nine variations, the final solidification can be seen forming in the feeder system. Moreover, the eighth variation demonstrates a more uniform solidification in comparison to the others. Moreover, during the solidification process at 20.269 seconds, the thickest section near the feeder gate retains an orange color, indicating that it remains in a liquid metal state. However, there is still enough supply of material from the feeding system, indicated by a large red color, to fill the vacancies within the mold cavity.

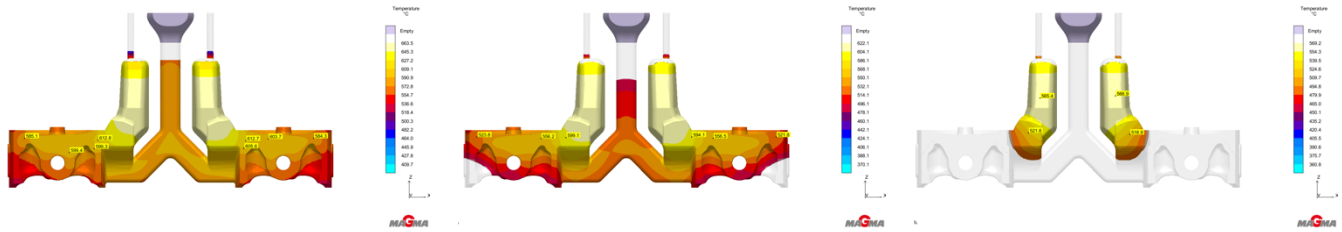

(a)

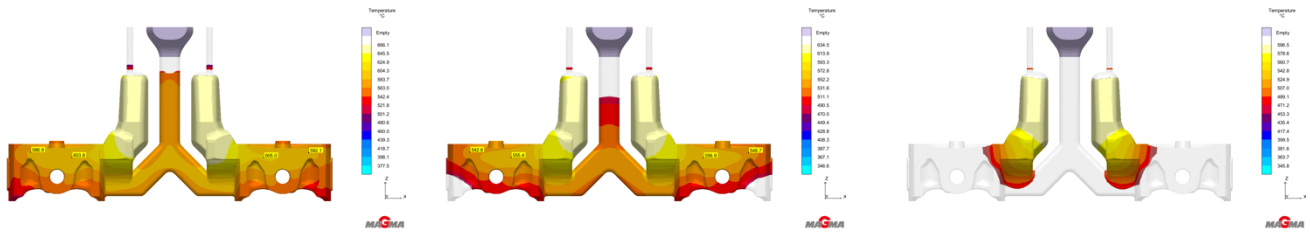

(b)

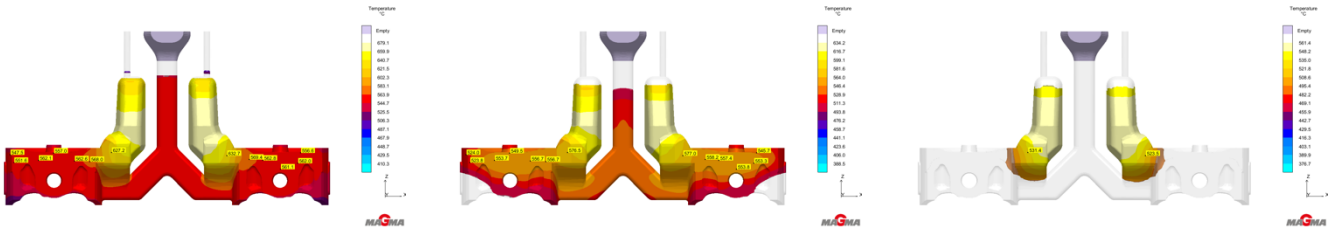

(c)

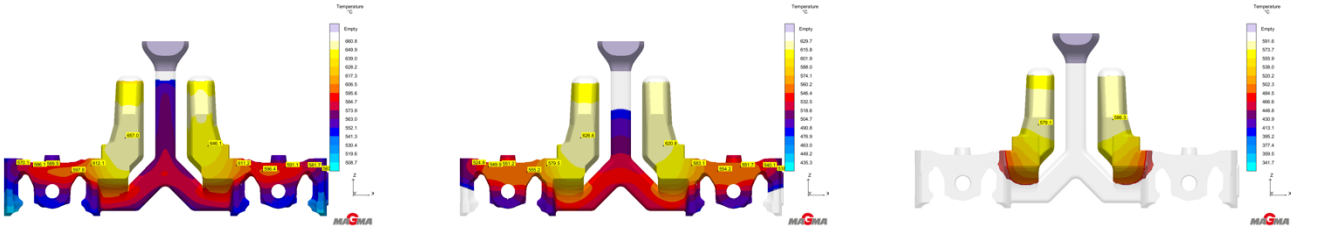

(d)

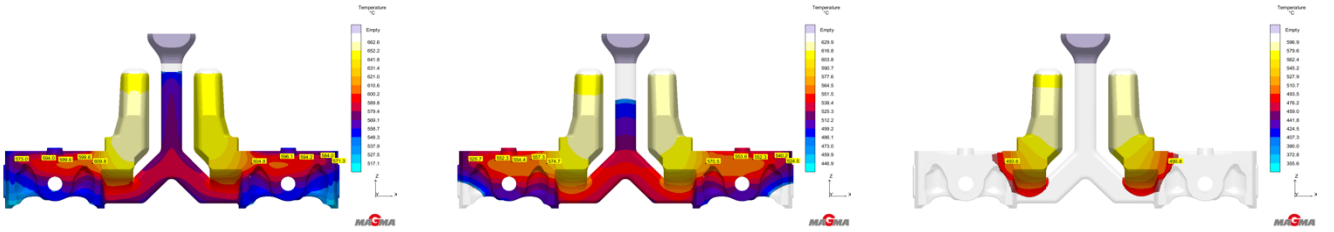

(e)

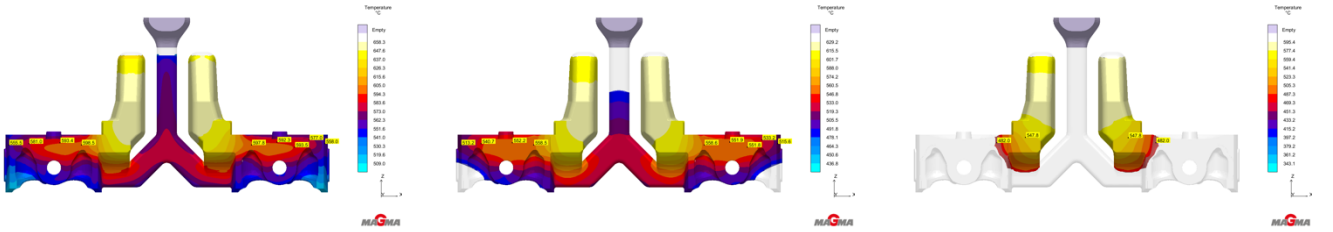

(f)

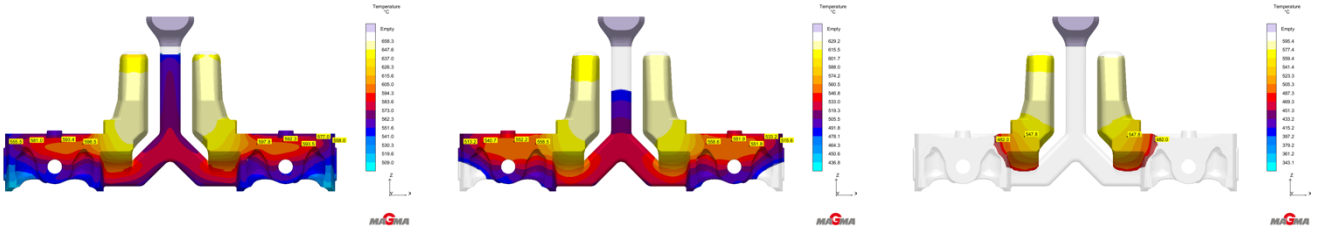

(g)

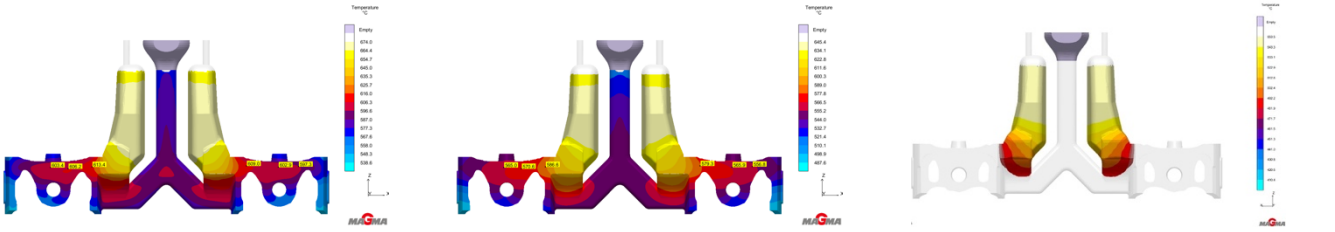

(h)

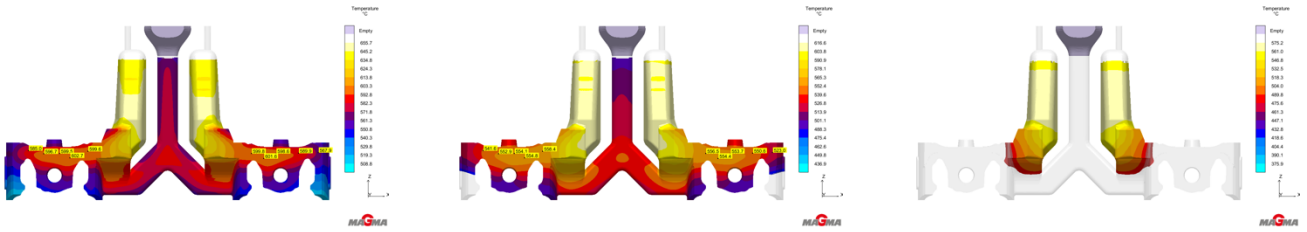

(i)

Figure 7. Distribution temperature of all designs (a) 1st variation, (b) 2nd variation (c) 3rd variation (d) 4th variation (e) 5th variation, (f) 6th variation, (g) 7th variation, (h) 8th variation, (i) 9th variation, observed at time intervals of 8.433 s, 20.269 s, and 88 s from left to right.

Figure 7 illustrates the distribution temperature (gradient temperature) during the solidification process. The image displays color variations indicating temperature changes from the initial pouring until the moment when the metal fills the whole mold. Analysis was conducted by observing temperature changes in regions susceptible to shrinkage porosity, namely the side core of the anti-feed gate, feed gate, and feeder sections at solidification times of 8.433 s, 20.269 s, and 88 s. Among the nine (9) variations examined, variation 8 demonstrates the most uniform temperature change at 88 seconds, indicating nearly complete solidification in the potentially defective areas. As depicted in Figure 7, these vulnerable areas have temperatures equivalent to the furthest section of the feeder system, specifically the side core of the anti-feed gate, which is approximately 500°C. Temperatures at the side core anti-feed gate consistently remain lower compared to the feed gate and feeder sections due to their contact with the mold. This phenomenon is associated with the higher thermal conductivity of the mold, facilitating quicker solidification when the molten metal, at high temperatures, comes into contact with the mold. Temperatures at the feed gate and feeder sections appear higher, approximately around 600°C. This indicates that the phase in these sections has not fully transitioned into solid form, thus still capable of filling voids in the mold cavity and consequently reducing the potential for shrinkage porosity.

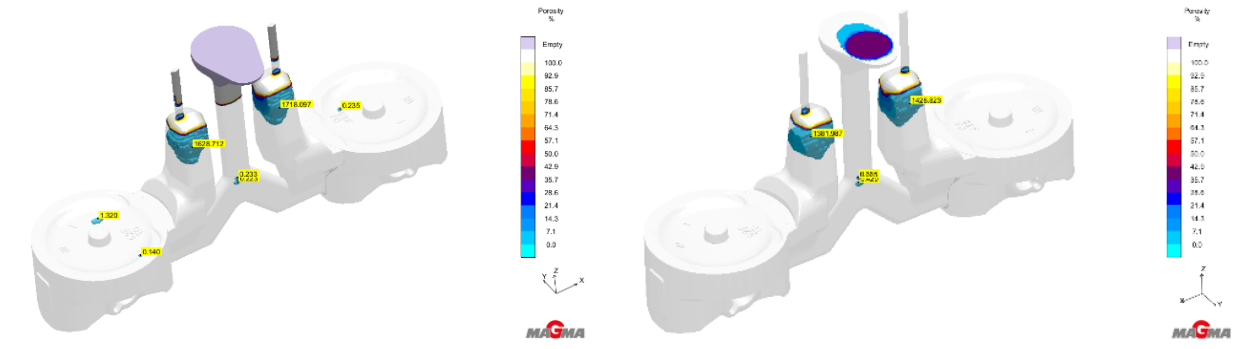

(a) (b)

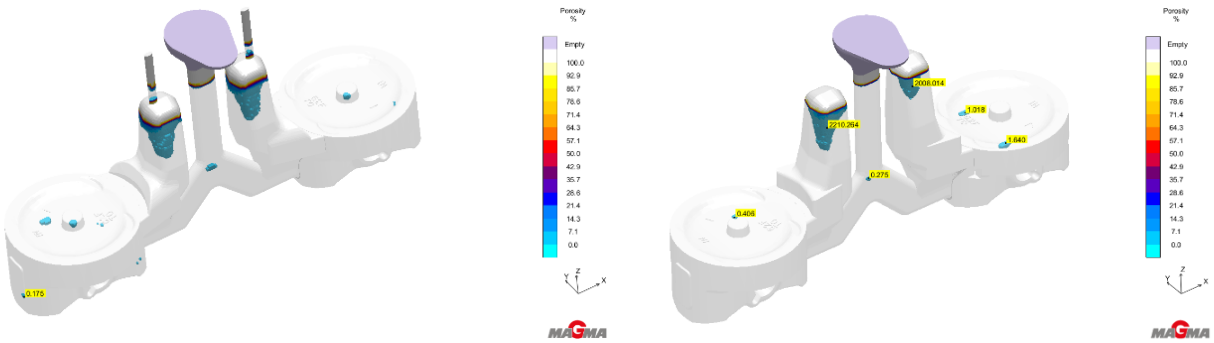

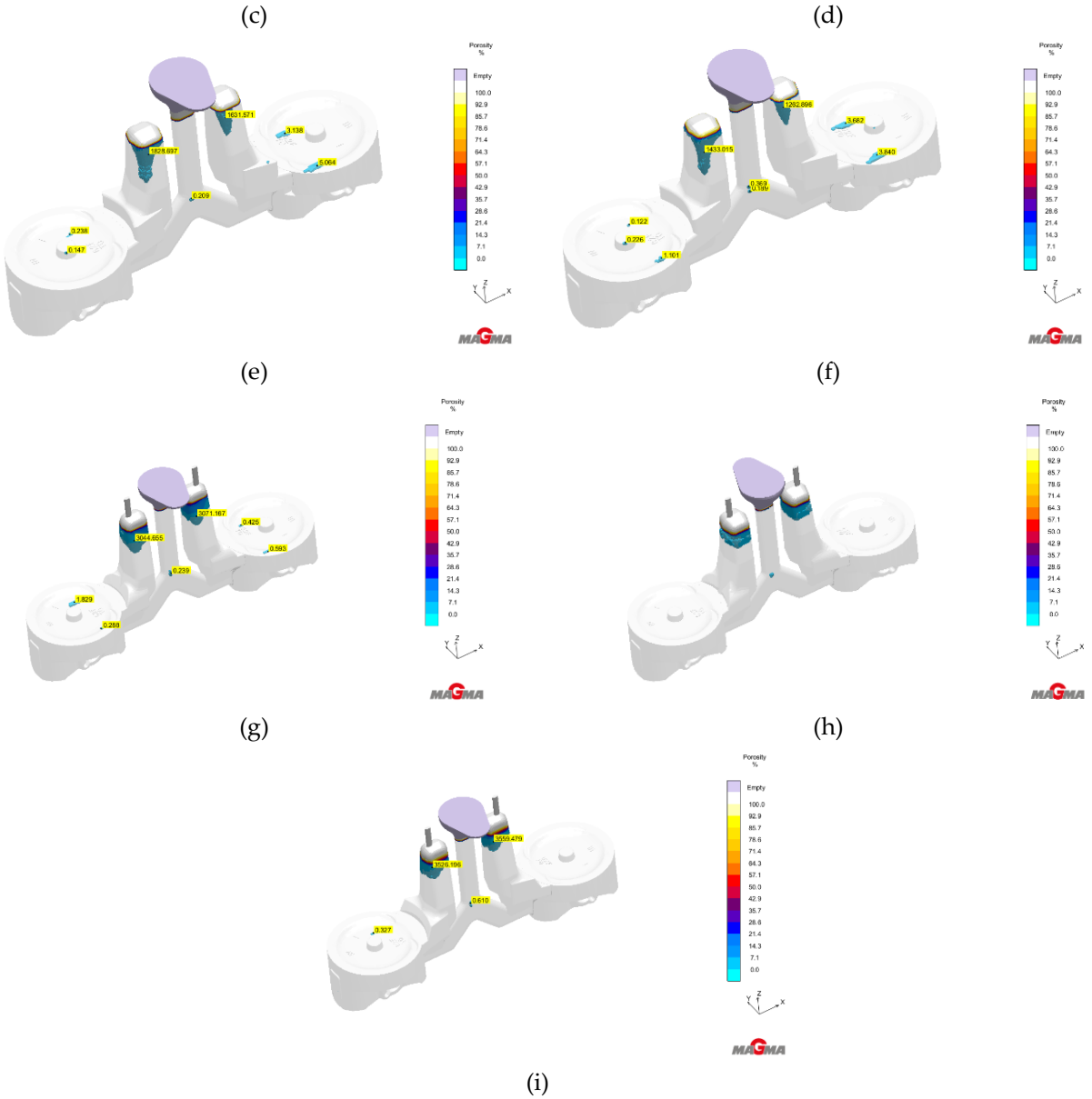

Figure 8. The position of shrinkage porosity of (a) 1st, (b) 2nd, (c) 3rd, (d) 4th, (e) 5th, (f) 6th, (g) 7th, (h) 8th, (i) 9th

Figure 8. illustrates the location and percentage of shrinkage for each variation tested. Shrinkage is more prevalent in the thickest sections than in other areas due to inadequate supply from the feeder system. As seen in Figure 8, integrating a feeder into the gating system facilitates the intake of additional material during the solidification process, effectively filling the reduced volume of molten metal in the mold. Consequently, the feeder serves as the final freezing point within the system. As a result, any shrinkage porosity that occurs will manifest in the feeder instead of the piston product. Among the nine (9) variations examined, variation 8 demonstrates that hot spots do not occur on the product, but are only found within the feeder system and its runner components. The porosity percentage values obtained from the analysis using Magmasoft 5.3 are presented in Table 3.

Table 3. The percentage and volume of shrinkage porosity for all tested variations

Var	Shrinkage prosity percentage (%)			Total Porosity (%)	Shrinkage porosity volume (mm^3)			Total shrinkage volume (mm^3)
	Runner	1st Cav	2nd Cav		Runner	1st Cav	2nd Cav	
1st	0.456	1.46	0.235	2.15	87.73	1240.78	199.71	1528.23
2nd	1.094	0	0	1.09	210.49	0.00	0.00	210.49
3rd	0.12	2.19	2.19	4.5	23.09	1861.17	1861.17	3745.43
4th	0.275	0.406	2.658	3.34	52.91	345.04	2258.90	2656.85
5th	0.209	0.385	8.202	8.79	40.21	327.19	6970.47	7337.87
6th	0.558	1.454	7.542	9.53	107.36	1235.68	6409.57	7752.61
7th	0.239	2.117	1.018	3.37	45.98	1799.13	865.15	2710.26
8th	0.758	0	0	0.76	145.84	0.00	0.00	145.84
9th	0.729	0.327	0	1.056	140.26	277.90	0.00	418.16

Table 3 illustrates the percentage and volume of Shrinkage Porosity in 9 variations of feeder size designs feeder size designs following simulation utilizing software feeder size designs following simulation utilizing Magmasoft. According to the table, the lowest porosity percentage is shown by the 8th variation, with a feeder height of 115 mm and feeder gate (ingate) of 45 mm, resulting in a shrinkage of 0.76% of the total casting product volume. The calculated volume of shrinkage porosity formed in the 8th variation is 145.84 mm^3 out of a total volume of 84985 mm^3. Furthermore, shrinkage porosity occurs in the runner rather than the product, where this part will not be used. The analytical results indicate that the width of the feeder gate has a significant impact on the occurrence of shrinkage. If the feeder width is too narrow, there will be an inadequate supply of molten metal to fill the empty spaces in the mold cavity during compaction. Nevertheless, if the size of the feeder gate is excessively large, it might induce an overabundance of material flow and a rapid flow rate, which can contribute to turbulence and subsequently cause shrinkage at multiple locations.

3.3. Dye Penetrant and Microstructural Analysis

To check the quality of cast products after simulation, the cast pistons were nondestructively tested using the dye penetrant method and microstructure analysis.

Initial Design

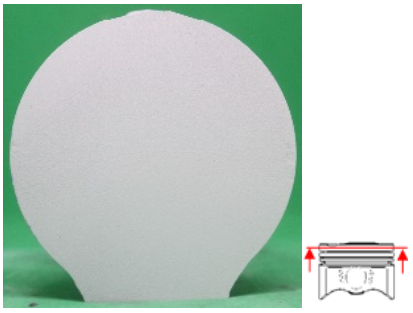

(a)

The 8th Variation

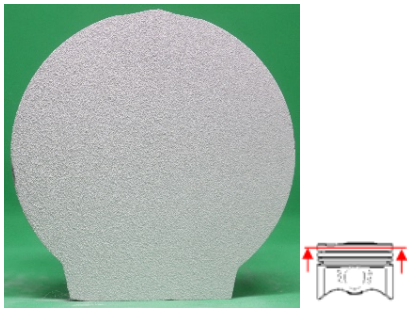

(b)

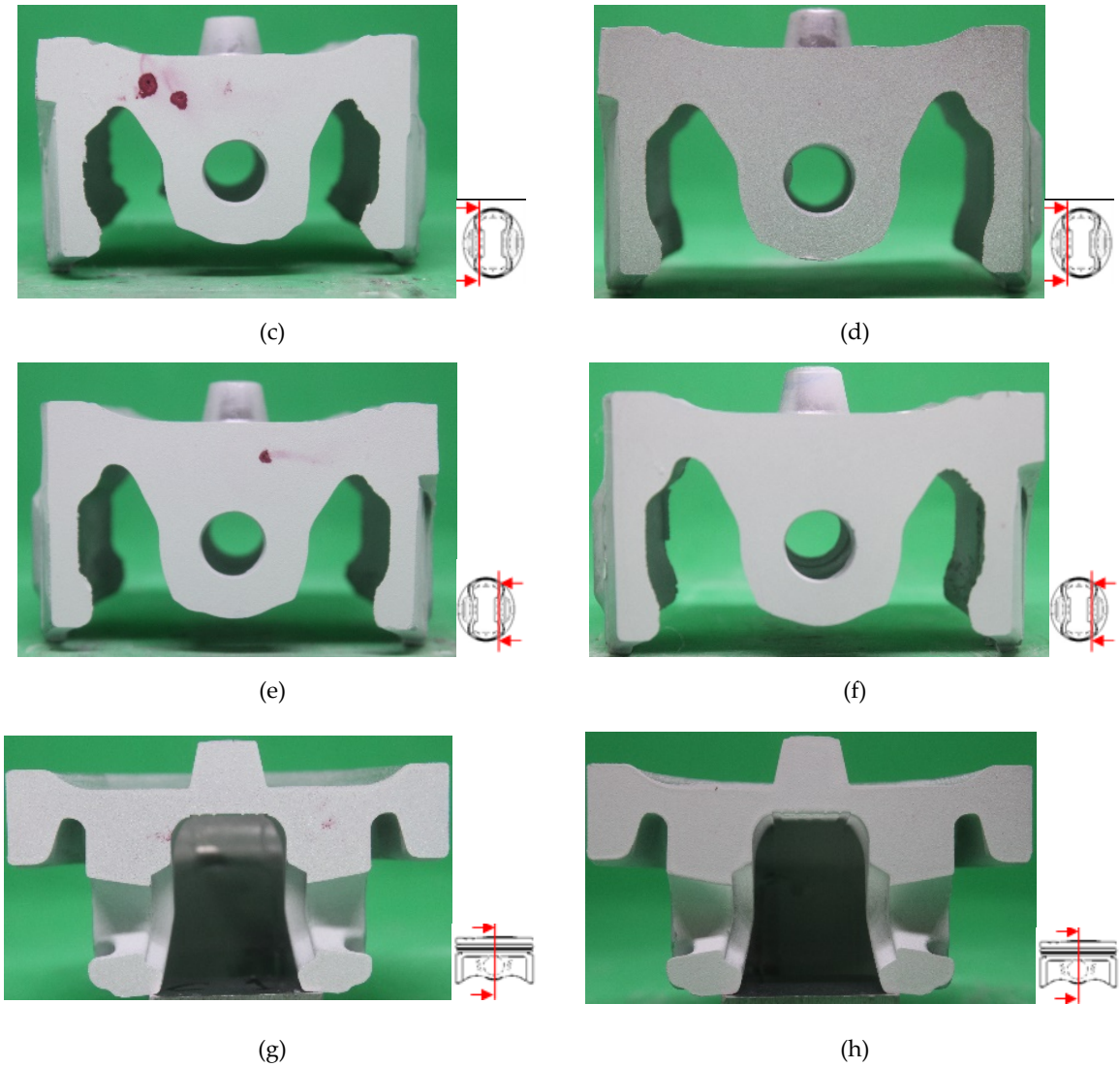

Figure 9. Comparison of dye penetrant test on (a) crown of initial design, (b) crown of 8th variation, (c) left side of pin-boss of initial design, (d) left side of pin-boss of 8th variation (e) right side of pin-boss of initial design (f) right side of pin-boss of 8th variation (g) pin center of initial design (h) pin center of 8th variation design

Figure 9. illustrates a comparison of the dye penetrant test results on the product before and after the modification of the gating system (8th variation). Among the nine variations tested in this study, variation eight emerged as the optimal configuration, featuring a feeder height of 115 mm and a feeder gate width of 44 mm. This particular variation resulted in a porosity percentage of 0.76% as determined by Computer-Aided Engineering (CAE) analysis. As can be seen in Figure 9, complete casting using the initial design exhibits porosity in the pin boss and pin center, as indicated by the red color observed by penetrant testing. This was due to the initial design producing the cooling process that led to the failure of timely feeding of molten metal. Moreover, the high thickness of the piston product is also a contributing factor to the occurrence of more shrinkage porosity. However, dye penetrant observation of the piston cast obtained from the 8th variation shows no porosities emerging within the product. This phenomenon is in good

agreement with the Magma simulation results, which indicated that the shrinkage porosity was only about 0.76% and primarily located in the feeder system and its runner components. As a result, the simulation accuracy in Figure 8 (h) is highly confirmed.

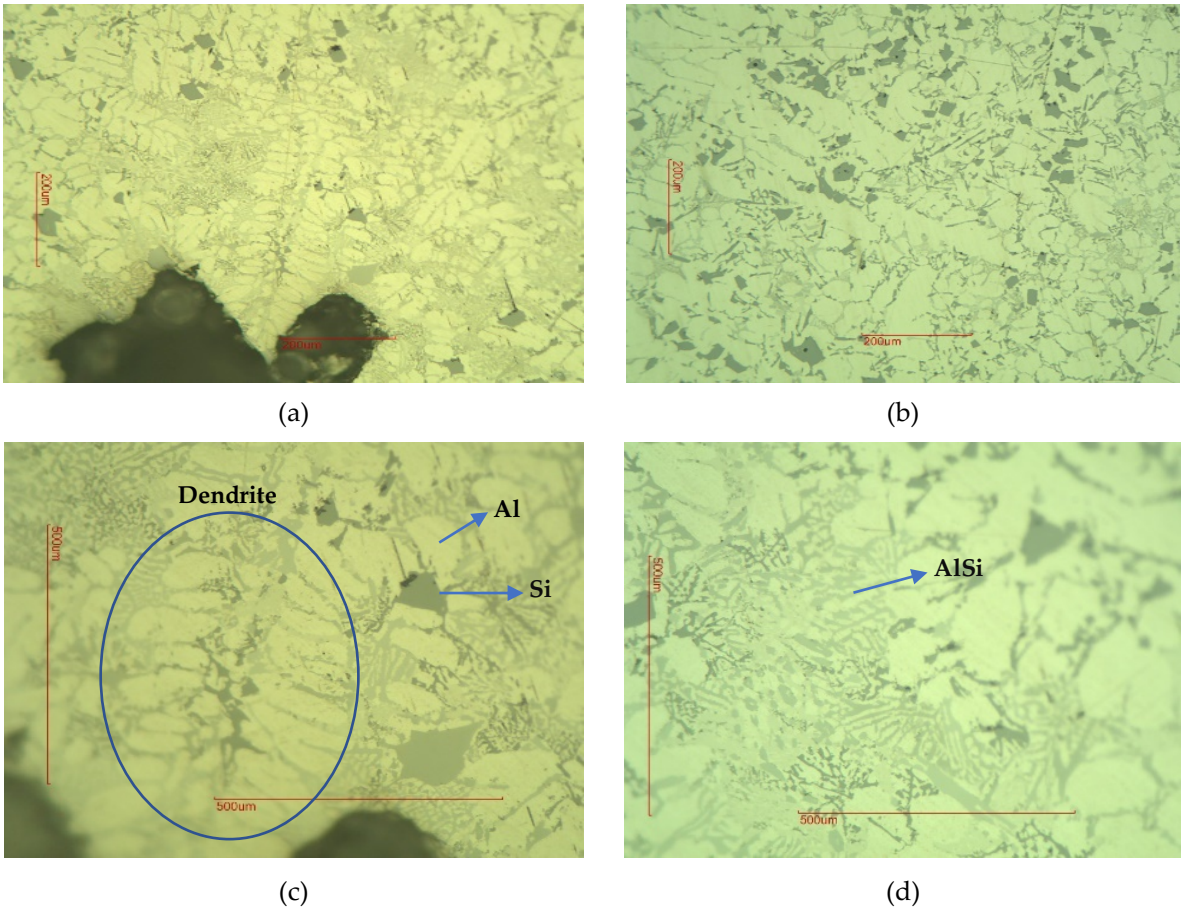

Figure 10. The optical micrographs depict the microstructures of the pin boss of the casting piston acquired from the original design of the gating system

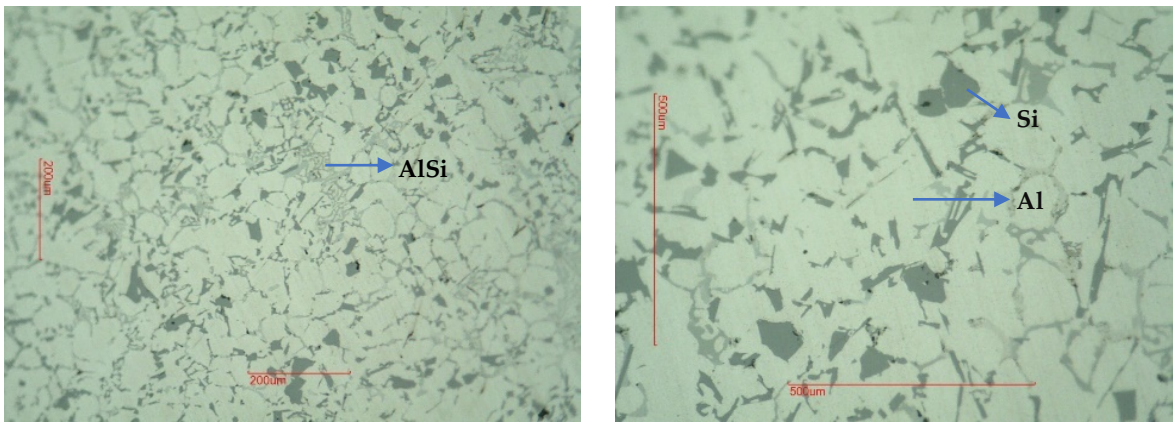

Figure 11. The optical micrographs depict the microstructures of the pin boss of the casting piston acquired from the 8th variation design of the gating system

Figure 10. displays the microstructure, revealing the shrinkage porosity of a cast piston utilizing a feeder system with dimensions of 90 mm in height and 32 mm in width. The microstructure exhibits a shrinkage porosity defect covering an area of 15,945.278 mm^2, which accounts for 17.378% of the total examined area. The impractical system of the cooling process in the initial design result in the failure to provide molten AC8A alloy adequately. The significant difference in thickness within the pin center and pin boss parts contributes to an increased occurrence of shrinkage porosity. This essentially confirms the accuracy of the simulation results. Moreover, Figure 11. reveals the microstructure of a piston product in the absence of shrinkage porosity. In general, the microstructure of both unmodified and modified gating systems consists of primary α-Al phase, primary Si, and eutectic Al-Si[26]. In addition, the major α-Al phase displayed two distinct forms: larger Al grains that developed in the shrinkage porosity due to slower cooling rates, and smaller Al grains that formed in the remaining sections with faster cooling rates. The larger Al grains exhibited dendritic or rosette-like morphology, as illustrated in Figure 10(c), whereas the smaller Al phase exhibited more equiaxial grains, as depicted in Figure 11(b).

4. Conclusions

In this study, a set of AlSi12CuNiMg gravity die-casting experiments has been conducted to solve the problem of shrinkage porosity in the cast piston industry. The analysis using a Computer-Aided Engineering (CAE) approach with the MagmaSoft numerical simulation on the effects of feeder height and feeder gate on the piston product led to the following conclusions:

1. An inadequate dimension of feeder height and feeder gate will result in an insufficient flow volume supply to the product. According to the simulation results, the maximum shrinkage porosity defect of 9.53% was generated at a feeder height of 106 mm and a feeder gate width of 48 mm. The microstructure analysis confirmed the existence of dendrites in the vicinity of the shrinkage porosity.
2. The most optimal variation was found to be a feeder height of 115 mm and a feeder gate width of 45 mm, which resulted in a shrinkage porosity of 0.76% in gating system.

References

1. B. Bhedasgaonkar, Casting Defect Analysis using Design of Experiments (DoE) and Computer Aided Casting Simulation Technique, Procediassure aluminum alloy casting, Journal of Materials Research and Technology 28 (2024) 4488–4497. https://doi.org/https://doi.org/10.1016/j.jmrt.2023.12.270.
2. B. Dybowski, A. Kiełbus, Ł. Poloczek, Effects of die-casting defects on the blister formation in high-pressure die-casting aluminum structural components, Eng Fail Anal 150 (2023) 107223. https://doi.org/https://doi.org/10.1016/j.engfailanal.2023.107223.
3. R. Wang, Y. Zuo, Q. Zhu, X. Liu, J. Wang, Effect of temperature field on the porosity and mechanical properties of 2024 aluminum alloy prepared by direct chill casting with melt shearing, J Mater Process Technol 307 (2022) 117687. https://doi.org/https://doi.org/10.1016/j.jmatprotec.2022.117687.
4. S. Bhagavath, Z. Gong, T. Wigger, S. Shah, B. Ghaffari, M. Li, S. Marathe, S. Karagadde, P.D. Lee, Mechanisms of gas and shrinkage porosity formation in solidifying shear bands, J Mater Process Technol 299 (2022) 117338. https://doi.org/https://doi.org/10.1016/j.jmatprotec.2021.117338.
5. D.R. Gunasegaram, D.J. Farnsworth, T.T. Nguyen, Identification of critical factors affecting shrinkage porosity in permanent mold casting using numerical simulations based on design of experiments, J Mater Process Technol 209 (2009) 1209–1219. https://doi.org/https://doi.org/10.1016/j.jmatprotec.2008.03.044.

6. S.L. Nimbulkar, R.S. Dalu, Design optimization of gating and feeding system through simulation technique for sand casting of wear plate, Perspect Sci (Neth) 8 (2016) 39–42. https://doi.org/https://doi.org/10.1016/j.pisc.2016.03.001.
7. H. Bhatt, R. Barot, K. Bhatt, H. Beravala, J. Shah, Design Optimization of Feeding System and Solidification Simulation for Cast Iron, Procedia Technology 14 (2014) 357–364. https://doi.org/10.1016/j.protcy.2014.08.046.
8. H. Iqbal, A.K. Sheikh, A. Al-Yousef, M. Younas, Mold Design Optimization for Sand Casting of Complex Geometries Using Advance Simulation Tools, Materials and Manufacturing Processes 27 (2012) 775–785. https://doi.org/10.1080/10426914.2011.648250.
9. T. Wang, S. Yao, Q. Tong, L. Sui, Improved filling condition to reduce casting inclusions using the submerged gate method, J Manuf Process 27 (2017) 108–113. https://doi.org/https://doi.org/10.1016/j.jmapro.2017.01.013.
10. D.G. Eskin, Suyitno, L. Katgerman, Mechanical properties in the semi-solid state and hot tearing of aluminium alloys, Prog Mater Sci 49 (2004) 629–711. https://doi.org/https://doi.org/10.1016/S0079-6425(03)00037-9.
11. D.M. Stefanescu, Computer simulation of shrinkage related defects in metal castings – a review, International Journal of Cast Metals Research 18 (2005) 129–143. https://doi.org/10.1179/136404605225023018.
12. E. 'Giller, N. 'Rensing, P. 'Zavracky, Method for producing high quality optical parts by casting, US20060192307A1, 2006.
13. R. Kumar, S. Madhu, K. Aravindh, V. Jayakumar, G. Bharathiraja, A. Muniappan, Casting design and simulation of gating system in rotary adaptor using procast software for defect minimization, Mater Today Proc 22 (2020) 799–805. https://doi.org/https://doi.org/10.1016/j.matpr.2019.10.156.
14. C. Lei, Y. Yang, G. Yang, Y. Huang, Magma software simulation assisted optimization of the casting system of turbocharger castings, Procedia Manuf 37 (2019) 59–65. https://doi.org/https://doi.org/10.1016/j.promfg.2019.12.013.
15. C.M. Choudhari, B.E. Narkhede, S.K. Mahajan, Casting Design and Simulation of Cover Plate Using AutoCAST-X Software for Defect Minimization with Experimental Validation, Procedia Materials Science 6 (2014) 786–797. https://doi.org/https://doi.org/10.1016/j.mspro.2014.07.095.
16. K. Chen, X. He, Z. Liu, G. Li, P. Zhang, H. Liu, Porosity forming mechanism and numerical simulation of casting process optimization of nickel-based heat-resistant alloy electrode ingot with large height to diameter ratio, Journal of Materials Research and Technology 29 (2024) 2363–2375. https://doi.org/https://doi.org/10.1016/j.jmrt.2024.01.211.
17. G. Timelli, G. Camicia, S. Ferraro, R. Molina, Effects of grain refinement on the microstructure, mechanical properties and reliability of AlSi7Cu3Mg gravity die cast cylinder heads, Metals and Materials International 20 (2014) 677–686. https://doi.org/10.1007/s12540-014-4013-2.
18. H. Yang, S. Ji, D. Watson, Z. Fan, Repeatability of tensile properties in high pressure die-castings of an Al-Mg-Si-Mn alloy, Metals and Materials International 21 (2015) 936–943. https://doi.org/10.1007/s12540-015-5108-0.
19. M. Vlach, J. Čížek, V. Kodetová, T. Kekule, F. Lukáč, M. Cieslar, H. Kudrnová, L. Bajtošová, M. Leibner, P. Harcuba, J. Málek, V. Neubert, Annealing Effects in Cast Commercial Aluminium Al–Mg–Zn–Cu(–Sc–Zr) Alloys, Metals and Materials International 27 (2021) 995–1004. https://doi.org/10.1007/s12540-019-00499-6.
20. K. Min, K. Kim, S.K. Kim, D.-J. Lee, Effects of oxide layers on surface defects during hot rolling processes, Metals and Materials International 18 (2012) 341–348. https://doi.org/10.1007/s12540-012-2020-8.
21. R. Haghayeghi, E. Ezzatneshan, H. Bahai, L. Nastac, Numerical and experimental investigation of the grain refinement of liquid metals through cavitation processing, Metals and Materials International 19 (2013) 959–967. https://doi.org/10.1007/s12540-013-5008-0.
22. S. Yue, G. Wang, F. Yin, Y. Wang, J. Yang, Application of an integrated CAD/CAE/CAM system for die casting dies, J Mater Process Technol 139 (2003) 465–468. https://doi.org/https://doi.org/10.1016/S0924-0136(03)00506-5.

23. L. Patnaik, I. Saravanan, S. Kumar, Die casting parameters and simulations for crankcase of automobile using MAGMAsoft, Mater Today Proc 22 (2020) 563–571. https://doi.org/https://doi.org/10.1016/j.matpr.2019.08.208.
24. U.A. Dabade, R.C. Bhedasgaonkar, Casting Defect Analysis using Design of Experiments (DoE) and Computer Aided Casting Simulation Technique, Procedia CIRP 7 (2013) 616–621. https://doi.org/https://doi.org/10.1016/j.procir.2013.06.042.

RiESTech
Recent in Engineering Science and Technology

MBI

Article

Hydro-Catalytic Cracking of Biomass Tar Contamination in Syngas

Aris Warsita [1], Hasta Kuntara [2], Zainal Abidin [3]

[1] Department of Mechanical Engineering, Insititut Teknologi Nasional Yogyakarta, Jl. Babarsari Caturtunggal, Depok, Sleman, 55281 Yogyakarta, Indonesia
[2] Department of Mechanical Engineering, Universiti Sains Malaysia Penang, Malaysia
* Correspondence: ariswarsita@itny.ac.id

Abstract: This paper describes new tar removal augmentation method by adding water that enhances the steam reformation reactions and converts tar contamination in the gas into combustible gases. The hydro-catalytic tar removal method was experimentally evaluated in a microwave-heated reactor with toluene and naphthalene as tar models. The reactor was tested in a wide temperature range with flow residence time through the reactor in the range of 0.12-0.24s. Dolomite and nickel catalysts were tested at 700-900°C while Y-zeolite, ruthenium, and rhodium were tested at 500-700°C temperature ranges. Steam-to-carbon ratio (S/C) was tested in the range of 0.11-0.55. Tar removal efficiency of 98.88% was achieved with ruthenium catalyst at 700 °C cracking temperature and S/C ratio range of 0.32-0.33. The gas product from tar cracking was analysed using gas chromatography and it consisted mostly of H2, CH4 and some higher hydrocarbon gases.

Keywords: Hydro-catalytic tar removal; Microwave irradiation; Thermal tar cracking; Naphthalene conversion; Toluene conversion

Citation:. Warsita, A., Kuntara, H., Abidin., Z. (2024). Hydro-Catalytic Cracking of Biomass Tar Contamination in Syngas. Recent in Engineering Science and Technology, 2(02), 18–34. Retrieved from https://www.mbi-journals.com/index.php/riestech/article/view/51

Academic Editor: Iwan Susanto

Received: 18 March 2024
Accepted: 6 April 2024
Published: 30 April 2024

Publisher's Note: MBI stays neutral with regard to jurisdictional claims in published maps and institutional affiliations.

1. Introduction

The conversion of solid biomass fuel into more convenient synthesis gas (syngas) with its neutral effect on global warming has been elaborately investigated for many decades [1,2]. Biomass syngas, unlike another type of renewable energy resources, can be utilized directly in most of the existing power plants without major modification by co-firing with fossil fuels. This option has been considered in many countries due to its positive effect on large scale electrical generation carbon footprint reduction. However, one of the major obstacles in syngas utilization is its high tar contamination that can cause blockage and fouling in fuel-feeding equipment. Moreover, tar has negative effect on fuel cells, reciprocating internal combustion (IC) engine and gas turbines in the long-term operation causing corrosion and fouling that can reduce engines life and increase maintenance cost [3,4]. Although steam boilers have higher tolerance to tar contamination, IC engines and gas turbines are sensitive to tar contamination and can accept only below 100 and 5 mg Nm^{-3} respectively [5]. Therefore, in subsequent utilization of syngas fuel, tar must be eliminated by converting it into useful gases.

Tar removal technology can be divided into two groups: removal inside the gasifier known as the primary method and the removal after the gasifier known as the secondary method [6]. Primary method is one of the oldest techniques of tar cracking and it has the advantage of eliminating any tar removal equipment after the gasifier, but with limited tar elimination capability [7,8]. On the other hand, heating, catalytic reaction and mechanical separation using a cyclone, filter and scrubber are common means of the secondary tar removal method.

Catalytic tar cracking with steam reforming during the gasification process is widely investigated [9,10]. Wide range of catalytic materials were tested in the primary method such as Ni, Al, Ru, Rh, Pt, Pd, Al_2O_3, ZrO_2, TiO_2, SiO_2, MOR1, CeO_2, ZrO_2 and MgO [11,12]. Dolomite is widely used as a non-metallic catalyst for the conversion of tar [13-15]. Dolomite calcination treatment is essential to achieve good tar conversion activity [16], and the effect also depends on the source of the natural dolomite [17,18]. However it has a low friction resistance and is easy to be carried away making it unfit for use in fluidized bed reactors. Olivine is another natural mineral which has shown higher activity in tar conversion [13,19]. When compared with dolomite, olivine has a high friction resistance which allows its direct use as the primary catalyst in fluidized bed gasifiers. The use of Y-zeolite for the conversion of biomass tar has also been reported but to a lesser extent [20-22].

As for the secondary tar removal in a separate reactor after the gasifier, the use of catalysts require temperature range of 500-900 ^{0}C making it more attainable both technically and economically. Also, tar is converted into combustible gases such as H_2, CH_4 and CO that enhances the quality of syngas. Various catalyst types such as Fe, Cu, Co and Ni based catalysts, dolomite, olivine and Y-zeolite were widely investigated [23-25].

Microwave irradiation is an alternative heating method which has been successfully applied to biomass pyrolysis [26,27]. Compared with conventional heating where heat is transferred from the surface to the core of the material by conduction driven by the temperature gradient, microwaves induce heat at the molecular level by direct conversion of electromagnetic energy into heat [28]. and results in uniform heating for particulate material. Another advantage is instantaneous response for fast microwave start-up and shutdown.

Microwave assisted thermal and catalytic syngas tar cracking has been widely investigated as well. Dolomite, Y-zeolite [29,30], bio-char [31] and bio-char with K and Ca [32] catalysts, as well as silicon carbide (SiC) [29, 30, 33] as micro wave radio frequency absorbing material have been studied. Most of the studies used tar model materials to simulate the different grades of biomass tar for better control over the quantities of tar with only few studies on actual tar from biomass gasification [30]. Common materials used as tar models are toluene, naphthalene, phenol, benzene, and 1-Methylnaphthalene [29-36].

In the current study, a new concept of hydro-catalytic tar removal in a post-gasification syngas treatment was experimentally investigated. The combined effect of water and catalytic materials in microwave assisted thermal cracking is fully characterized. Wide range of catalysts: dolomite, Y-zeolite, nickel, ruthenium, and rhodium were tested separately with different water-tar ratios to obtain maximum tar removal.

2. Materials and Experiment Methods

2.1. Materials and Catalytic Calcination

In this study, actual syngas from biomass gasification was not used to evaluate the methods of tar removal due to the continuous fluctuation in tar concentration. Therefore, toluene and naphthalene (commercial grade) tar models were used for better control and accurate measurement of tar removal. Naphthalene ($C_{10}H_8$) is a lightweight poly-aromatic hydrocarbons (LPAH) consists of two fused benzene rings and it is a class 4 tar while toluene (C_7H_8) is a light aromatic hydrocarbon (LAH) with a ring compound which is a class 3 tar. Both classes 3 and 4 tar are classified as the main tar products from biomass

gasification in fluidized bed and downdraft gasifiers. Purified nitrogen (99.999%) was used as a carrier gas to transfer tar model vapours through the tar cracking reactor.

Tar formed in the pyrolysis zone inside the gasifier is one of the main sources of tar, thus, catalytic pyrolysis has attracted much attention as a promising potential in tar reduction [35]. However, catalytic materials have to go through calcination process at elevated temperature to achieve the desired effect. In this study, five catalytic materials: dolomite, Y-zeolite, nickel, ruthenium and rhodium were investigated for tar removal. Commonly, the use of support materials for nickel catalyst such as alumina, zeolite, dolomite and olivine has been widely studied in literatures due to their positive effect on tar removal as well as increasing the pore size and surface area. However, pure nickel was used in this study to provide more controlled environment to test its effect on tar cracking without any support materials. Dolomite has a particle size of 600 μm with a bulk density of 1.33 g cm^{-3}. It is mainly composed of 34.69 wt.% CaO, 15.06 wt.% MgO and 2.34 wt.% SiO_2. Y-zeolite is a commercial catalyst powder (CBV720) with a bulk density of 0.26 g cm-3 and SiO_2/Al_2O_3 of 30. Commercial nickel 257 553, Aldrich is a mix of metal, with a thickness of 0.5 mm, bp 2733 ^{0}C, mp 1453 ^{0}C and density of 8.9 g/ml at 25 ^{0}C. Commercial ruthenium 246047-72-3 with $C_{46}H_{65}C_{12}N_2PRu$, and 848.97 $g.mol^{-1}$. Commercial rhodium $C_{17}H_{18}NORh$ 33409-86-3, and has a molecular weight of 355.24 $g.mol^{-1}$. The process of making natural dolomite included grounding and sieving with output particle sizes in the range of 0.2-0.5 mm, followed by calcination. Calcination of dolomite is needed for high tar decomposition activity since it has large surface area and oxide content on the surface. H_2 content in the producer gas can be more improved with the use of calcined dolomite as downstream catalytic steam gasification compared to that of uncalcined dolomite [37]. The effect of calcination was widely in literatures as reviewed by Anis and Zainal [6] and has shown a positive improvement in catalyst activity. A muffle oven with air flow was used for dolomite and nickel calcination at 900 ^{0}C for 1 hour and at 600 ^{0}C for 2 hours for Y-zeolite,

ruthenium and rhodium. Table 1 shows the catalytic materials specifications and calcination processes.

Table 1. Characteristics of catalysts

Properties	Value	Properties	Value
Y-zeolite		**Ruthenium**	
SiO_2/Al_2O_3	30	assay	99.98% trace metals basis
Na_2O	0.03% (wt.%)	form	powder and chunks
Unit cell size (Å)	24.28	Calcination	600 °C for 2h under air flow
Surface Area	780 (m^2/g)	**Rhodium**	
Pore size (Å)	7.4	assay	99.95% trace metals basis
density	0.26 (g m^{-3})	form	powder
Calcination	600 °C for 2 h under air flow	resistivity	4.33 $\mu\Omega^{-cm}$ at 20 °C
Dolomite		density	12.41 g/cm^3
Composition (wt.%)	34.69% CaO, 15.06% MgO, 2.34% SiO_2, 1.07% Al_2O_3, 0.61% Fe_2O_3	Calcination	600 °C for 2 h under air flow
Particle size	600 (μm)		
density	1.33 (g m^{-3})		
Calcination	900 °C for 1h under air flow		
Nickel			
assay	99.7% trace metals basis		
form	powder		
resistivity	6.97 $\mu\Omega^{-cm}$, 20 °C		
particle size	<50 μm		
density	8.9 g/mL at 25 °C		
Calcination	900 °C for 1h under air flow		

Carbon based susceptor materials has the ability to absorb radio frequency and convert it into heat. Charcoal is one of the commonly used susceptor materials. However, it was not used in this study due to its additional effect as a catalyst that will interfere with the measurement of the catalytic effect of other materials. Silicon carbide (SiC) was used instead as the susceptor material. Four SiC particle sizes were compared: 2.085mm (F10), 1.765 mm (F12), 1.470 mm (F14) and 1.230 mm (F16) to investigate the effect of particle sizes on radio frequency penetration depth and heat generation.

2.2. Experimental Procedures and Equipment

The experimental test rig was developed in a previous study to investigate the hydrothermal cracking of tar without catalysts. The experimental test rig consists of the tar vapour/steam generator, mixing chamber, ceramic tube reactor, microwave oven and tar/gas sampling train. Four type-K thermocouples are used for temperature measurement at different parts of the system as shown in Figure 1. A predetermined tar/water mass is placed in a stainless steel (SS) insulated container for tar evaporation and steam generation. LPG stove is used to provide the required heat for boiling, and the temperature is maintained at 250°C throughout the test to achieve homogenous mixing between tar and steam. Pressurized nitrogen is used as a carrier gas to control the flow residence time through the reactor. In order to insure the mixture homogeneity, tar vapour/steam flow is mixed with nitrogen in a SS insulated mixing chamber, and the temperature is maintained at 200°C

using hot-plate induction heater. Details of the system design and the tar/gas sampling train were published [38].

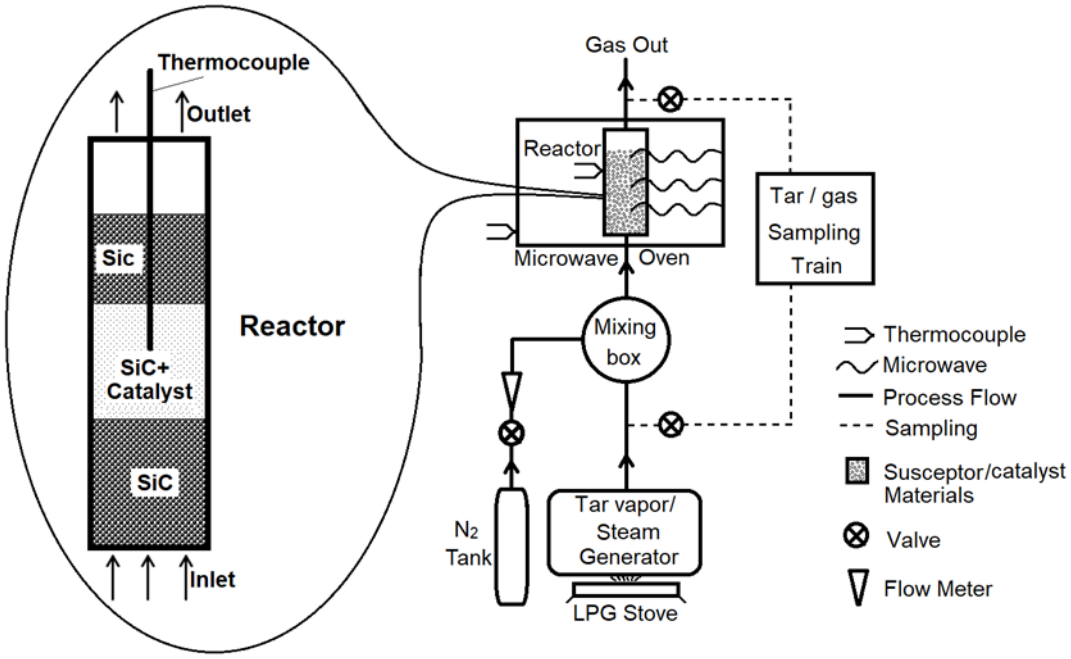

Figure 1. Schematic diagram of the experiment test rig

In this investigation, three sets of experiments were performed. First, the rector was characterised with SiC as the reactor bed material by passing N_2 carrier gas only without the addition of water, tar and catalytic materials. Four main variables were compared: SiC particle size, bed height, N_2 flow rate, and microwave electrical input power. Power absorption efficiency of the microwave oven was calculated as the ratio of the actual absorbed power by the bed material to the electrical power input. The absorbed power (Pabs) is calculated according to Equation (1) [39]:

$$\boldsymbol{P_{abs} = \rho c_p \frac{(T - T_{inlet})}{t} V + h_i A (T - T_{inlet}) + \varepsilon \sigma A \bar{T}^4} \quad \textbf{(1)}$$

where T, Tinlet and T¯ are the reaction temperature (K), reactor inlet temperature (K) and the average temperature within the reactor (K), respectively whilst t is the irradiation time period (s), r is the density of absorber material (kg m^{-3}), cp is the heat capacity of absorber material (J kg^{-1} K^{-1}), hi is the convective heat transfer coefficient (W m^{-2} K^{-1}), ◎ is the emissivity of absorber material and ◎ is Stefan-Boltzman constant (5.67 x 10-8 W m^{-2} K^{-4}) and A is the reactor wall surface area.

The second set of experiments investigated the effect of water addition on tar cracking with different types of catalytic materials. In order to provide a controlled environment, all the catalysts were used in their pure form as an active catalyst without the addition of any promoter or support materials to increase the pore size or surface area and enhance tar cracking. Therefore, nickel and other metals were used in their pure form without any support materials. This will reduce naturally their performance due to their non-pours nature and lower surface area.

Tar cracking efficiency was calculated as the ratio of mass of the tar model obtained from the tar sampling train before and after passing the reactor. Main investigated variables for each catalyst were the steam-to-carbon (S/C) mass ratio and cracking temperature in the

range of 500-900 ^{0}C. S/C ratio was chosen over the water-to-tar ratio used in other studies [38] due to the variation in carbon mass % in tar as it presents 93.8% in naphthalene compared to 91.3% in toluene. The tested S/C ratio values for toluene were 0.11, 0.22, 0.33, 0.44, 0.55 and for naphthalene were 0.1, 0.21, 0.32, 0.43, 0.53.

The third set of experiments included the analysis of the gas product from the reactor at different cracking temperatures. Different types of catalytic materials were tested with the optimum S/C ratio obtained from the second set of experiments. The gas product is basically generated by the thermal catalytic cracking of the tar model additional to the steam reactions. Gas compositions and heating value were determined using gas chromatography (GC). The experiments provided the optimum operation conditions to achieve maximum heating value of the gas product.

2.3. Tar Hydro-Catalytic Cracking

The use of thermal cracking as the only mean for tar cracking is not efficient due to the lack of oxygen content in the light aromatic and light poly-aromatic hydrocarbons that are classified into classes 3 and 4 tar mainly from downdraft gasifiers. Thus, using catalysts containing free oxygen has shown positive effect on tar cracking and preventing coke formation [40]. Other than the free oxygen, CO_2 can also be used as an agent but in highly endothermic reactions. Equations (2⍟6) show the common reactions associated with the reduction of tar using O_2 and CO_2 agents [41,42].

Oxidation: $C + O_2 \leftrightarrow CO_2 + 393$ kJ.mol-1 (2)

Partial oxidation: $C + 1/2O_2 \leftrightarrow CO + 110$ kJ.mol-1 (3)

Boudouard reaction: $C + CO_2 \leftrightarrow 2CO -$ 173.8 kJ.mol-1 (4)

Dry reforming: $CH4+CO_2 \leftrightarrow 2CO+2H_2 -$ 247.3 kJ.mol-1 (5)

Methanation: $C + 2H_2 \leftrightarrow CH_4 +74.82$ kJ.mol-1 (6)

Steam gasification can produce syngas with a considerably higher heating value compared to air gasification which is mainly cause by the increment in H_2 concentration in the product gas. Similarly, the addition of water at elevated temperature inside the reactor initiates steam reaction with tar that produces H_2 [43] as illustrated in Equations

(7◎11) [36]. Tar model also cracks into methane that reacts with water in steam reforming reactions as shown in Equations (12, 13) forming H2 as part of the gas product from the reactor. Toluene and naphthalene steam reforming reactions:

$$C_7H_8 + 7H_2O \rightarrow 7CO + 11H_2 \quad (7)$$

$$C_{10}H_8 + 10H_2O \leftrightarrow 10CO + 14H_2 \quad (8)$$

Heterogeneous water gas reaction: $C + H_2O \leftrightarrow CO + H \quad -118.9\ kJ.mol^{-1}$ (9)

$$C + 2H_2O \leftrightarrow CO_2 + 2H_2 - 90.2\ kJ.mol^{-1} \quad (10)$$

Homogeneous water gas shift reaction: $CO + H_2O \leftrightarrow CO_2 + H_2 + 40\ kJ.mol^{-1}$ (11)

Methane steam reforming reactions:

Primary: $CH_4 + H_2O \leftrightarrow CO + 3H_2 - 206.3\ kJ.mol^{-1}$ (12)

Secondary: $CH_4 + 2H_2O \leftrightarrow CO_2 + 4H_2 - 165\ kJ.mol^{-1}$ (13)

It can be noticed that CO formation is mainly through endothermic reactions either by the steam or dry reforming reactions or the Boudouard reaction. Thus, reaction sustainability and equilibrium is highly dependent on the heat supply to the reaction and reaction temperature.

2.4. Tar and Product Gas Analysis

Tar samples before and after the passing the reactor were condensed at 22 ^{0}C in the sampling train while gas product after the reactor was collected in gas sampling bags. Gas product was analysed using GC model CP 4900 with a thermal conductivity detector (TCD). Tar samples were analysed using gas chromatography/mass spectrometry (GC-MS) model 7890-5975C Agilent with HP-5 MS capillary column. Helium was used as carrier gas at a flow rate of 1.2 mL/min. The size was 1 μL injection with a split ratio of 1:10.40 ^{0}C initial oven temperature was held for 3 minutes and then increased to 290 ^{0}C at a rate of 5 ºC/min, and held at 290 ^{0}C for 5 minutes while the injector and detector were maintained at a constant temperature of 230-250 ^{0}C.

For gas product, H^2, CO, CO^2, CH_4 and N_2 gas concentrations were detected by GC while the C_2-C_3 hydrocarbons were not detected. Nitrogen flow rate was always fixed during the tests, thus, the change in the average N2 concentration was determined by calculating the results of H_2, CO, CO^2 and CH_4 concentration in each time trial. Based on the product

gas, the conversion of toluene (xC_7H_8) was calculated according to Equation (14) in terms of carbon in the product gas (CO, CO_2, CH_4)p divided by the carbon in toluene.

$$\mathbf{X}_{\boldsymbol{c}} = \frac{[\boldsymbol{CO}]\boldsymbol{p} + [\boldsymbol{CO_2}]\boldsymbol{p} + [\boldsymbol{CH_4}]\boldsymbol{p}}{\mathbf{7}[\boldsymbol{C_7H_8}]\boldsymbol{inlet}} \quad (14)$$

An example of the calculation of hydrogen product by the potential stoichiometry corresponding to the total conversion of toluene into H_2 is shown in Equation (15), where hydrogen concentration [H_2] is taken from GC results. Other gases are calculated similarly.

$$[\boldsymbol{H_2}]\boldsymbol{p} = [\boldsymbol{H_2}] \times \mathbf{18}[\boldsymbol{C_7H_8}]\boldsymbol{inlet} \quad (15)$$

Sulfur-compounds contamination in gas product such as H_2S are prominent in coal gasification with sulfur deposits issues on the catalyst surfaces that can lead to catalyst deactivation. However, this issue is nearly prevented by biomass gasification with low sulfur contamination, thus, sulfur-compounds were not considered in this study.

3. Results and Discussion

Preliminary set of experiments included the thermal characterization of the reactor and the optimum operation conditions of the reactor were utilized for tar removal optimization. The most effective catalyst and the optimum S/C ratio were used subsequently to characterize the tar reduction and product gas quality.

3.1. Thermal Characteristic of Microwave Reactor

The aim of these set of experiments was to obtain the optimum thermal cracking conditions for the reactor without including tar models and catalytic materials. The main tested reactor variables were: SiC particles sizes, SiC bed height, N2 gas flow rate, microwave input power.

3.1.1.Effect of absorber material particle size

Four SiC particle sizes were tested while fixing other variables at 700 W input power, 10 LPM N_2 flow rate, and maximum bed height of 120 mm. Figure 2a shows the power absorption efficiencies for each absorber bed material particle sizes. Results showed that the average absorption efficiencies were 87%, 88%, 91% and 93% for F10, F12, F14 and F16 sizes, respectively. In general, the difference was less than 5% on average, indicating that for all particle sizes, the microwave energy was enough to penetrate into the particles and might only focus on one hotspot. Since SiC absorber particle size of F16 provided good efficiency and temperature, this size was used in subsequent experiments.

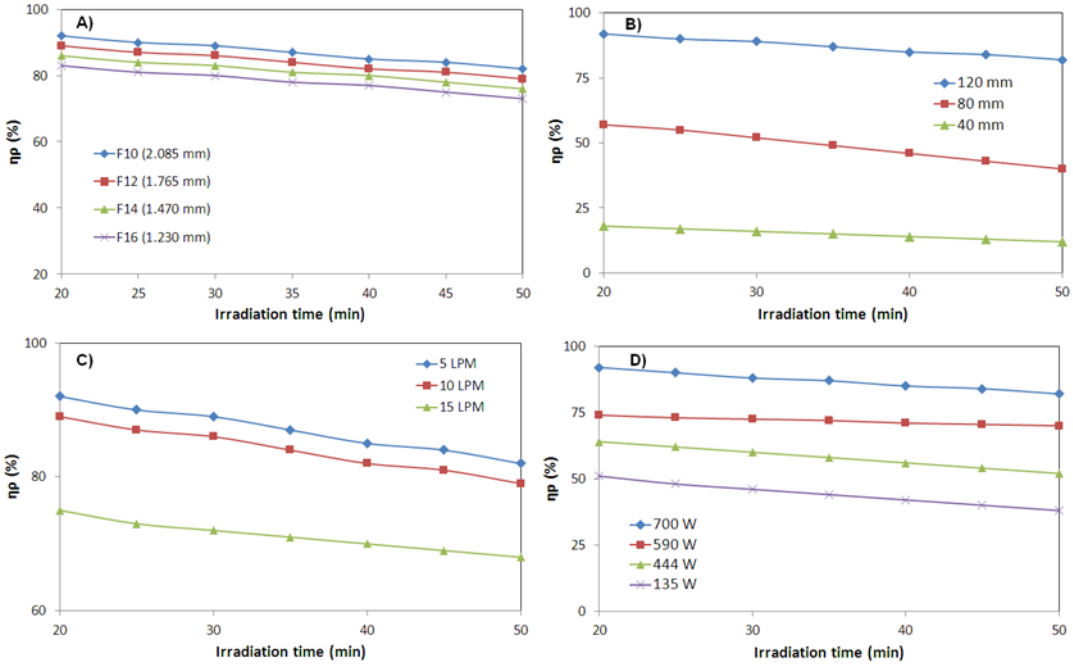

Figure 2. Power absorption efficiency for different: (a) SiC particle size, (b) SiC bed height, (c) gas flow rate, and (d) microwave input power

3.1.2.Effect of bed height

The effect of SiC bed height on the microwave oven power absorption efficiency was further characterized while fixing other variables at 10 LPM N_2 flow rate, F16 SiC particle size and 700 W power input. The absorption efficiencies were calculated with three bed heights as shown in Figure 2b. As expected, the absorption efficiency improved significantly as the volume of absorber bed material increased. It was found that the average power absorption efficiencies for bed heights of 40, 80 and 120 mm were 15%, 43% and 87%, respectively. Thus, it can be concluded that for lower bed height/volume, only a small portion of the emitted microwave power to the absorber material can be absorbed and converted into heat. On the other hand, increasing the height of the bed materials is limited by the reactor geometry and also by the elevation in flow pressure drop. SiC bed height of 120 mm was used in all subsequent experiments. Further increase of bed height was not possible due to the limitation of reactor size used in this work.

3.1.3.Effect of gas flow rate

Another significant variable is the gas flow rate through the reactor since it governs the residence time. Bed particle size or bed porosity usually affects directly the flow rate when low-pressure blower is used, due to the flow restriction. However, with pressurized N_2 used as the carrier gas, the pressure drop effect was eliminated. The effect of various N_2 flow rates in the range of 5 - 15 LPM were investigated while fixing other variables such as the maximum bed height of 120 mm, F16 SiC particle size and 700 W power input as shown in Figure 2c. It can be noticed that lower gas flow rate resulted in higher power absorption efficiency. This phenomenon can be explained by the heat balance within the reactor in which the microwave power dissipation into heat from the absorber material surface was still able to overcome the heat losses especially by convection. On the other hand, for high flow rates the flow cooling effect was significant causing a drop in temperature and absorption efficiency. The results show that the average power absorption efficiencies for gas flow rates of 5, 10 and 15 LPM were 92%, 87% and 66%, respectively. In

general, the required residence time for tar cracking will be the main factor that determines the suitable gas flow rate. However, these results give an insight on the flow rate effect on absorption efficiency where gas flow rates below 15 LPM is recommended to obtain better heating.

3.1.4.Effect of microwave power

The input power of the microwave is the primary variable that dictates the absorption power hence the absorption efficiency. Other variables were fixed at optimum values of 120 mm bed height, 10 LPM N_2 flow rate, and particle size of F16. Figure 2d shows the power absorption efficiency for different microwave input powers. The average absorption efficiencies for 135, 444, 590 and 700 W input powers were respectively around 41%, 54%, 67% and 87%. The rapid heating effect and fast temperature elevation at higher input powers resulted in a significant enhancement of the absorption efficiency compared to the low power operation.

It can be concluded that input power and bed height have more influence on power absorption efficiency followed by the gas flow rate then the bed particles sizes. Also a slight reduction in the absorption efficiency with time was noticed as a common trend for all the variables due to the slight changes in the absorber material properties with temperature elevation.

3.2. Effect of Catalyst and Water Addition on Tar Removal

Sufficient removal of tar contamination in biomass syngas using only heat supply from the microwave oven will require a significant temperature elevation up to 1200 ^{0}C. This might be not feasible both technically and economically in many large scale gas cleaning applications. Adding water has shown a considerable enhancement in tar removal efficiency, but high temperature was still a requirement [36]. Adding catalysts has been proven to achieve good tar cracking at much lower temperatures and hence, lower power input requirement. In this study, dolomite, Y-zeolite, nickel, ruthenium, and rhodium catalytic materials were all tested separately with S/C ratios in the range of 0.1- 0.5 and temperature range of 500-700 ^{0}C.

Figure 3 shows the removal efficiency for toluene and naphthalene with the various catalysts. The optimization temperature was limited to a relatively low cracking temperature of 700 ^{0}C rather than the maximum tested temperature of 900 ^{0}C. The lower temperature is more attainable from the practical point of view since the catalytic materials can be placed right after the throat in downdraft gasifiers where gas temperature is still around 700 ^{0}C before it cools down at the gasifier exit. This eliminates the need for external heating for the tar cracking purpose. Steam addition triggers the water-gas shift reaction, even at lower reaction temperatures due to the low energy required for the activation, and the reaction increases H_2 and CH_4 concentrations in the gas. On the other hand, steam reforming reaction requires higher energy for the activation and the inclusion of this reaction in the overall reaction equilibrium is limited and depends on the local temperature of the reactants.

Increasing S/C ratio contributed positively to the tar removal for all the catalysts up to 0.33 ratio. However, further increase in steam flow showed the opposite effect on tar cracking. This could be attributed to the coke formation at higher steam flow rates as early studies in literature reported the increase of coke deposits on catalyst surface resulted from the steam reforming reaction at lower temperatures [44]. The type of catalyst also plays a major role in the resistance toward coke formation on the surface that can lead eventually to the catalyst deactivation.

Therefore, an adequate presence of steam to initiate tar cracking through the water-gas shift as the main reaction and partially through the steam reforming reaction was found to be at S/C ratio in the range of 0.32-0.33 for toluene and naphthalene. Further increase of steam flow increased the steam reformation activation in the global equilibrium. This resulted in the formation of coke deposits on the catalysts surfaces with noticeable degradation in the tar cracking performance. The most effective catalyst was ruthenium followed by nickel. Average toluene removal efficiencies for the optimum condition for the catalysts were: 97.27% for dolomite, 96.04% for Y-zeolite, 96.55% for rhodium, 98.76% for nickel, and 98.88% for ruthenium. As for naphthalene, the effect of the catalyst type was nearly identical to that of toluene with both having similar number of hydrogen atoms. However, with naphthalene being heavier than toluene, the maximum naphthalene removal efficiency was slightly lower of 96.9%.

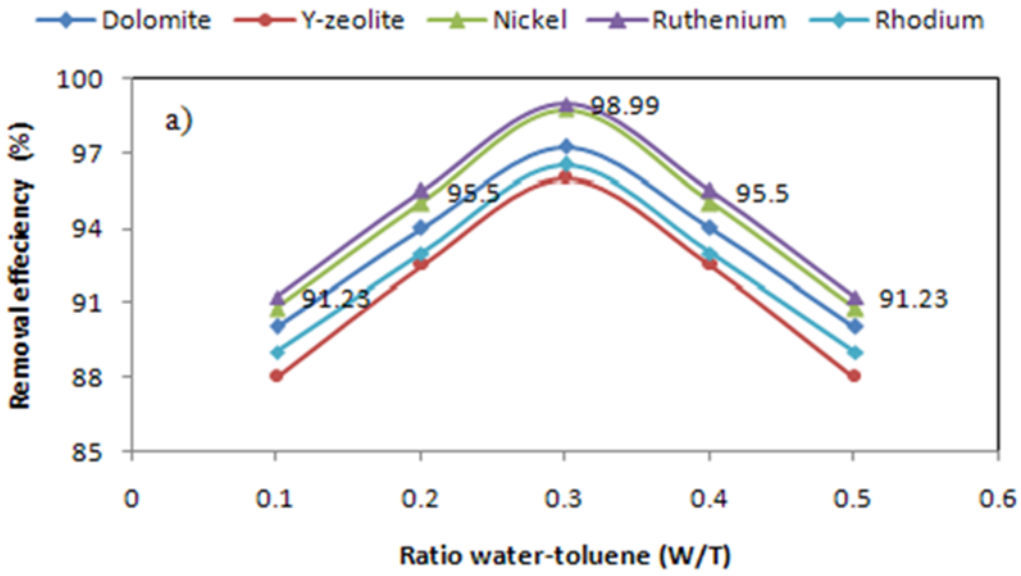

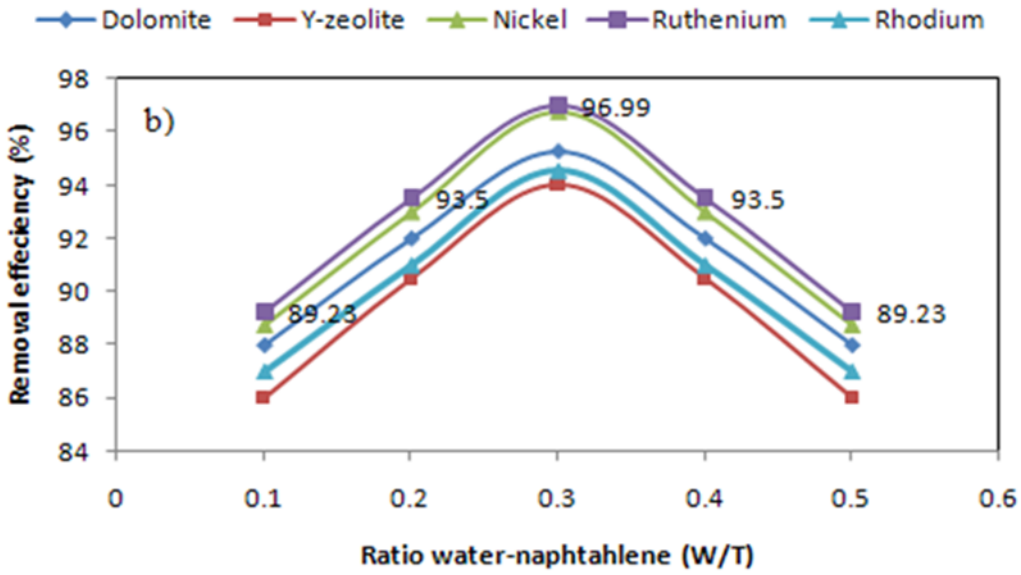

Figure 3. The effect of water addition on tar removal efficiency with various types of catalysts for toluene and naphthalene

Tar removal efficiencies were compared for the cases with S/C ratio range of 0.32-0.33 and without any water addition with all the catalysts at 700 ^{0}C as shown in Figure 4. It can be noticed that naphthalene which is class 4 tar was much harder to crack compared to the lighter toluene, a class 3 tar in all the cases. Also, up to 4.9% enhancement in removal efficiency for both naphthalene and toluene were achieved by adding the optimum amount of water to the reaction with ruthenium.

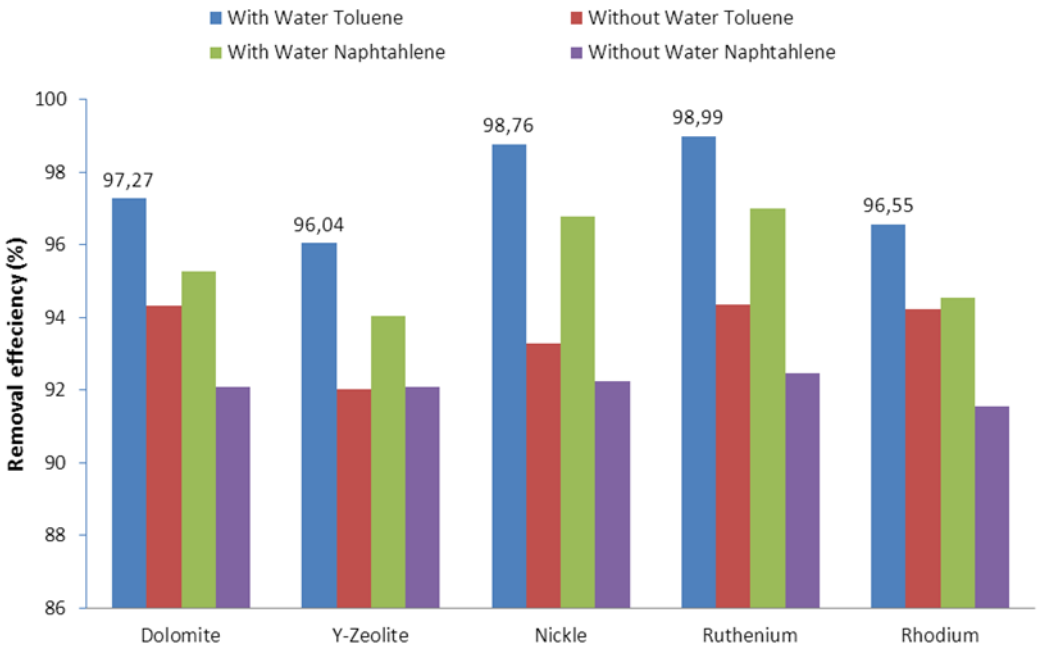

Figure 4. Removal efficiency of tar models with different type of catalysts at 700 ^{0}C and residence time of 0.24s

Most of the tar model was converted into a gas product inside the reactor, while the remaining condensable tar was collected in the sampling train and analysed using GC-MS. Table 2 shows the species mass concentrations of the remaining condensable tar reduced from toluene after the catalytic thermal treatment with ruthenium and water in the temperature range of 500-700 ^{0}C. It was found that most of toluene mass was converted into different tar species during thermal treatment except for the samples treated at 700 ^{0}C where 45% of toluene remained in the sample. This finding is slightly different to the detected tar species in the case of dolomite at 700 ^{0}C in which phenanthrene, styrene and chrysene were not identified in the case of ruthenium at 500 ^{0}C. In addition, most of the heavy PAHs were decomposed at reaction temperature of 500 ^{0}C, meaning that the ruthenium catalyst inhibited the formation of high-ring tar compounds. This activity was due to Y-zeolite catalyst contained sufficient acidic active sites on its surface thereby accelerated tar cracking reaction. Moreover, by increasing the catalytic reaction temperature up to 700 ^{0}C, it can be seen that the catalytic activities of ruthenium increased significantly. At this condition, benzene, toluene, o-xylene, indene, methylindene and naphthalene were the only major compounds identified.

Table 2. Tar sample compound and composition resulting from ruthenium catalytic treatment of model tar toluene

Compound name	Molecular weight	Boiling point (°C)	Tar sample composition after cracki			
			Ruthenium catalyst reaction temper			
			500	550	600	650
Benzene	78	80	11.45	9.57	14.35	10.69
Toluena	92	110.6	13.63	11.19	12.15	16.93
Ethylbenzene	106	145	0.85	0.87	-	-
p-Xylene	106	138.3	1.31	1.80	1.94	2.95
o-Xylene	106	144.5	2.87	3.62	4.65	6.59
Benzene, (1-methylethyl)-	120	172.8	0.19	0.16	-	-
Indene	116	182	6.54	6.50	7.27	2.82
Methylindene	130	199	7.87	11.04	4.88	4.69
Naphthalene	128	217.9	4.27	6.39	6.54	7.90
2-Methylnaphthalene	142	241.1	3.01	5.84	4.88	5.66
1-Methylnaphthalene	142	244.7	2.10	5.88	4.33	2.61
4-Butyl-1,1'-biphenyl	210	318	2.54	-	-	-
Anthracene	178	339.9	4.50	10.33	6.96	-
Methylenephenanthrene	190	353	4.03	5.71	7.17	-
Fluoranthene	202	384	3.23	5.71	4.44	-
Pyrene	202	404	6.29	8.22	11.75	26.00
11H-Benzo|b|fluorene	216	405	7.56	7.15	8.70	13.17
Pyrene, 1-methyl-	216	405	6.25	-	-	-
Acepyrene	226	448	11.48	-	-	-
Total			100	100	100	100

3.3. Gas Product Characteristics

The last set of experiments included the optimization of the gas product from toluene and naphthalene tar model compounds. Different types of catalysts were tested in the temperature range of 500 - 700 ^{0}C, gas residence time in the range of 0.12 - 0.24 seconds and optimum S/C ratio range of 0.32-0.33. It was found that dolomite and rhodium showed low toluene removal efficiency compared to Y-zeolite, nickel and ruthenium at the conditions investigated. Same goes for the removal of naphthalene that showed similar behaviour which is also in a good agreement with the findings of other researchers [27].

Differences in the catalyst activity were mainly due to the differences in their physical and chemical properties shown earlier in Table 1. The literature suggests that the average pore diameter of dolomite is generally above 600 μm while Y-zeolite has a pore size of about 7.4 μm [16]. On the other hand, toluene and naphthalene molecules are in the range of 0.49-0.73 μm. Thus, the porous structure of Y-zeolite, ruthenium and rhodium catalysts with larger pore size allows toluene and naphthalene to diffuse into the pores causing higher catalytic activity. Moreover, the high activity of these catalysts can also be contributed by its higher contact surface area, additional to the acidic nature of the catalysts that can also promote the removal of toluene and naphthalene. On the other hand, dolomite and nickel suffered from the non- porous structure that limited the contact surface area.

Toluene removal efficiency with different catalysts and gas products yield mainly H_2, CH_4 and higher HCs as shown in Figures 5 a-e. The removal of toluene was carried out in the temperature range of 700 - 900 ^{0}C for dolomite and nickel and 500-700 ^{0}C for Y zeolite, ruthenium, and rhodium. The lower removal efficiency with dolomite and nickel need

temperature elevation up to 900 ^{0}C to get higher efficiency comparable to the other catalysts. Soot was observed on dolomite and nickel surfaces with a small portion of the catalysts turned black, especially at the bottom. This can be explained by the higher pore size with less contact surface area for the reaction resulting in concentrated reaction hot spots. Also, Y-zeolite requires lower temperatures (maximum 700 ^{0}C) while the other catalyst materials have low Si/Al ratios such as A-, X and high ratio of Si/Al such as ZSM-5 that requires higher temperatures up to 1300 ^{0}C. Further increase in temperature showed no significant improvement in toluene removal for all the cases. The black grains and soot products decreased significantly with the increase in temperature during the toluene and naphthalene removal with Y zeolite, ruthenium, and rhodium. This is mainly due to the larger contact surface area for reaction and the acidic nature the catalysts.

Removal of toluene showed a significant improvement at higher temperatures for all catalysts. As for the gas production, a steady elevation in H_2 was noticed mainly due to the water addition through the steam reforming and water gas shift reactions. On the other hand, significant elevation in CH_4 production was noticed at higher temperatures mainly due to the cracking of higher HCs that converted eventually to H_2 and CH_4. This could also be partially attributed to the slower methane dry reforming reaction compared steam reactions [45] that reduced CH_4 conversion into H_2 and CO. The effect of catalytic materials used here on tar cracking can be put in the order from highest to lowest as following: ruthenium, nickel, dolomite, rhodium, and Y zeolite. In conclusion, the main factors contributed to the high efficiency tar removal were the intensive radio frequency heating, long residence time, high temperature and catalytic materials.

The use of catalytic materials inside the gasifier chamber for tar cracking has the advantage of the elevated temperature and the availability of steam released from the raw materials during the initial drying phase. However, this method suffers from the frequent deactivation of the catalysts caused by the coke and alkaline materials deposits on the catalyst surface. Tar contamination in gas product from updraft gasifiers occurs when gas passes through the relatively cooler pyrolysis and drying zones. Thus, tar contains mainly heavy oxygenated-based compounds and heterocyclic compounds presenting classes 1 and 2 which can be efficiently removed using second stage thermal cracking reactor. On the other hand, the oxygenated light tar compounds are cracked when the gas passes through the hot throat in downdraft gasifiers, leaving only tars of classes 3 and 4 in the gas. A combination of a catalyst with oxygen carrier materials can be placed at the gasifier throat exit with external steam stream at an adequate S/C ratio can be a promising solution since the gas temperature is still above 700°C. This will not only reduce the tar contamination, but also enhance the quality of the gas product by elevating the H_2 and CH_4 concentrations in the gas.

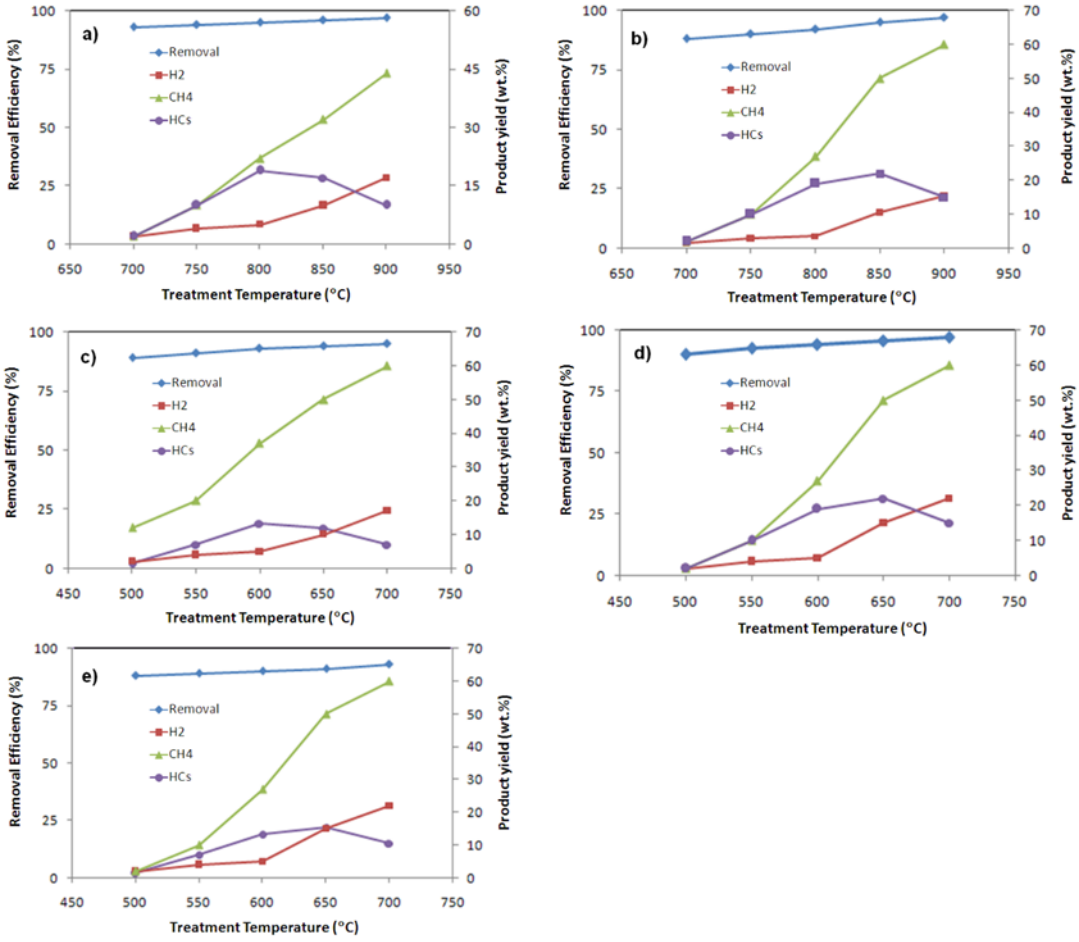

Figure 5. The final product during catalyst removal tar model of toluene with catalysts: (a) dolomite and (b) nickel (c) Y-zeolite, (d) ruthenium and (e) rhodium

4. Conclusions

Microwave assisted hydro-catalytic biomass tar cracking was experimentally investigated. The microwave reactor optimum operation condition were found to be 700 W input power, 120 mm bed height and 5LPM carrier gas flow rate with maximum power absorption efficiency of 87%. Optimum S/C ratio was in the range of 0.32-0.33 for naphthalene and toluene tar models with maximum tar removal efficiency of 98.88% with ruthenium catalyst at 700 °C. Gas product from tar cracking was characterized in the temperature range of 500–700 °C. CH_4 yield was above 50% with most of the catalysts and dropped with dolomite, while H_2 was about 20% for most of the catalysts and dropped with nickel.

Acknowledgments: The author would like to thank Universiti Sains Malaysia and FRGS 203/PMEKANIK/6071320 for the financial support of this work.

References

1. Al-attab KA, Zainal ZA (2017) Syngas production and combustion characteristics in a biomass fixed bed gasifier with cyclone combustor. Appl. Therm. Eng. 113, 714–721.
2. Grieco EM, Gervasio C, Baldi G (2013) Lanthanum–Chromium–Nickel Perovskites for the Catalytic Cracking of Tar Model Compounds. Fuel 103, 393–397.
3. Al-attab KA, Zainal ZA (2014) Performance of a biomass fueled two-stage micro gas turbine (MGT) system with hot air production heat recovery unit. Appl. Therm. Eng. 70, 61- 70.

4. Mastellone ML, Zaccariello L (2013) Metals Flow Analysis Applied to the Hydrogen Production by Catalytic Gasification of Plastics. Int. J. Hydrogen Energy 38, 3621–3629.
5. Ud Din Z, Zainal ZA (2016) Biomass integrated gasification–SOFC systems: Technology overview, Renewable Sustainable Energy Rev. 53, 1356–1376.
6. Anis S, Zainal, ZA. (2011) Tar reduction in biomass producer gas via mechanical, catalytic and thermal methods: A review. Renew. Sustain. Energy Rev. 15, 2355-2377.
7. Machin EB, Pedroso DT, Proenza N, Silveira JL, Conti L, Braga LB, Machin A B (2015) Tar reduction in downdraft biomass gasifier using a primary method. Renew. Energy 78, 478-483.
8. Zhang Y, Kajitani S, Ashizawa M, Oki Y (2010) Tar destruction and coke formation during rapid pyrolysis and gasification of biomass in a drop-tube furnace. Fuel 89, 302-309.
9. Zhang Z, Liu L, Shen B, Wu C (2018) Preparation, modification and development of Ni-based catalysts for catalytic reforming of tar produced from biomass gasification. Renewable and Sustainable Energy Reviews 94, 1086–1109.
10. Xu J, Holthaus P, Yang N, Jiang S, Heupel A, Schönherr H, Yang B, Krumm W, Jiang X (2019) Catalytic tar removal using TiO2/NiWO4-Ni5TiO7 films. Applied Catalysis B: Environmental 249, 155-162.
11. Sutton D, Kelleher B, Ross JR (2001) Review of Literature on Catalysts for Biomass Gasification. Fuel Process. Technol. 73, 155–173.
12. Asadullah M, Miyazawa T, Ito SI, Kunimori K, Yamada M, Tomishige K. (2003) Catalyst Development for the Gasification of Biomass In The Dual-Bed Gasifier. Appl. Catal., A. 255, 169–180.
13. Rapagná S, Provendier H, Petit C, Kiennemann A, Foscolo PU (2002) Development of Catalysts Suitable for Hydrogen or Syn-Gas Production from Biomass Gasification. Biomass Bioenergy 22, 377-388.
14. Taralas G, Kontominas MG (2006) Pyrolysis of Solid Residues Commencing from the Olive Oil Food Industry for Potential Hydrogen Production. J. Anal. Appl. Pyrolysis 76, 109–116.
15. Pérez-Martínez D, Giraldo SA, Centeno A (2006) Effects of The H2S Partial Pressure on The Performance of Bimetallic Noble-Metal Molybdenum Catalysts in Simultaneous Hydrogenation And Hydrodesulfurization Reactions. Appl. Catal., A. 315, 35–43.
16. [Aznar MP, Caballero MA, Sancho JA, Francés E (2006) Plastic Waste Elimination By Co-Gasification With Coal And Biomass in Fluidized Bed With Air in Pilot Plant. Fuel Process. Technol. 87, 409–420.
17. Gusta E, Dalai AK, Uddin MA, Sasaoka E (2009) Catalytic Decomposition of Biomass Tars with Dolomites. Energy Fuel 23, 2264–2272.
18. Devi L, Ptasinski KJ, Janssen FJ, Van Paasen SV, Bergman PC, Kiel JH (2005) Catalytic Decomposition of Biomass Tars: Use of Dolomite and Untreated Olivine. Renew. Energy 30, 565–587.
19. Chiang KY, Lu CH, Lin MH, Chien KL (2013) Reducing Tar Yield in Gasification of Paper-Reject Sludge by Using A Hot-Gas Cleaning System. Energy 50, 47–53.
20. Mun TY, Kim JS (2013) Air gasification of dried sewage sludge in a two-stage gasifier. Part 2: Calcined dolomite as a bed material and effect of moisture content of dried sewage sludge for the hydrogen production and tar removal. Int. J. Hydrog. Energy 38, 5235–5242.
21. Mun TY, Kim JW, Kim JS (2013) Air gasification of dried sewage sludge in a two-stage gasifier: Part 1. The effects and reusability of additives on the removal of tar and hydrogen production. Int. J. Hydrog. Energy 38, 5226–5234.
22. Ud Din Z, Zainal ZA (2017) The fate of SOFC anodes under biomass producer gas contaminants. Renew. Sustain. Energy Rev. 72, 1050–1066.
23. Chang JS (2003) Next Generation Integrated Electrostatic Gas Cleaning Systems. J. Electrostatic. 57 273–291.
24. Ribeiro AM, Santos JC, Rodrigues AE (2010) PSA Design for Stoichiometric Adjustment of Bio-Syngas for Methanol Production and Co-Capture of Carbon Dioxide. Chem. Eng. J. 163 355–363.

25. Bu Q, Lei H, Zacher AH, Wang L, Ren S, Liang J, Wei Y, Liu Y, Tang J, Zhang Q, Ruan R (2012) A Review of Catalytic Hydrodeoxygenation of Lignin-Derived Phenols from Biomass Pyrolysis. Bioresour. Technol. 124, 470–477.
26. Wang, L., Li, D., Koike, M., Koso, S., Nakagawa, Y., Xu, Y., Tomishige, K.: Catalytic Performance And Characterization of Ni-Fe Catalysts for The Steam Reforming of Tar From Biomass Pyrolysis To Synthesis Gas. Appl. Catal., A. 392, 248–255 (2011).
27. Farag S, Kouisni L, Chaouki J (2014) Lumped Approach in Kinetic Modeling of Microwave Pyrolysis of Kraft Lignin. Energy Fuels 28, 1406–1417.
28. Anis, S., Zainal, Z. A., Bakar, M. Z. A.: Thermocatalytic Treatment of Biomass Tar Model Compounds via Radio Frequency. Bioresour. Technol. 136, 117–125 (2013).
29. Anis S, Zainal ZA (2013) Upgrading producer gas quality from rubber wood gasification in a radio frequency tar thermocatalytic treatment reactor, Bioresour. Technol. 150, 328–337.
30. Li L, Song Z, Zhao X, Ma C, Kong X, Wang F (2016) Microwave-induced cracking and CO2 reforming of toluene on biomass derived char, Chem. Eng. J. 284, 1308–1316.
31. Feng D, Zhao Y, Zhang Y, Sun S, Meng S, Guo Y, Huang (2016) Effects of K and Ca on reforming of model tar compounds with pyrolysis biochars under H2O or CO2, Chem. Eng. J. 306, 422–432.
32. Bhattacharya M, Basak T (2016) A review on the susceptor assisted microwave processing of materials. Energy 97, 306◎338.
33. Radwan AM, Kyotani T, Tomita A (2000) Characterization of Coke Deposited from Cracking of Benzene over Usy Zeolite Catalyst. Appl. Catal., A. 192, 43–50.
34. Buchireddy PR, Bricka RM, Rodriguez J, Holmes W (2010) Biomass Gasification: Catalytic Removal of Tars Over Zeolites and Nickel Supported Zeolites. Energy Fuels 24, 2707–2715.
35. Anis S, Zainal ZA (2014) Study on kinetic model of microwave thermocatalytic treatment of biomass tar model compound, Bioresour. Technol. 151, 183–190.
36. Lv P, Chang J, Xiong Z, Huang H, Wu C, Chen Y, Zhu J (2003) Biomass Air−Steam Gasification in a Fluidized Bed to Produce Hydrogen-Rich Gas. Energy Fuels 17, 677–682.
37. Hu G, Xu S, Li S, Xiao C, Liu S (2006) Steam gasification of apricot stones with olivine and dolomite as downstream catalysts. Fuel Process. Technol. 87, 375-382.
38. Warsita A, Al-attab KA, Zainal ZA (2017) Effect of water addition in a microwave assisted thermal cracking of biomass tar models, Appl. Therm. Eng. 113, 722–730.
39. Cherbanski R, Molga E (2009) Intensification of desorption processes by use of microwaves—An overview of possible applications and industrial perspectives. Chem. Eng. Process. 48, 48–58.
40. Li C, Hirabayashi, D, Suzuki K (2009) A crucial role of O2 - and O2 2- on mayenite structure for biomass tar steam reforming over Ni/Ca12Al14O33. Appl. Catal. B: Environ. 88, 351-360.
41. Virginie M, Adánez J, Courson C, De Diego LF, García-Labiano F, Niznansky D, Kiennemann A, Gayán P, Abad A (2012) Effect of Fe–Olivine on The Tar Content During Biomass Gasification in A Dual Fluidized Bed. Appl. Catal., B. 121–122, 214–222.
42. Virginie M, Courson C, Kiennemann A (2010) Toluene Steam Reforming as Tar Model Molecule Produced During Biomass Gasification with An Iron/Olivine Catalyst. C. R. Chim. 13, 1319–1325.
43. Skoulou V, Kantarelis E, Arvelakis S, Yang W, Zabaniotou A (2009) Effect of Biomass Leaching on H2 Production, Ash And Tar Behavior During High Temperature Steam Gasification (Htsg) Process. Int. J. Hydrog. Energy 34, 5666–5673.
44. Trimm DL (1997) Coke formation and minimisation during steam reforming reactions. Catalysis Today, 37, 233-238.
45. Kajitani, S., Suzuki, N., Ashizawa, M. & Hara, S. 2006. CO_2 gasification rate analysis of coal char in entrained flow coal gasifier. Fuel, 85, 163-169.

RiESTech
Recent in Engineering Science and Technology

MBI

Article

IoT-based Intelligent Monitoring & Control System Planning Using Project Management Method and Business Feasibility Analysis

Muhammad Farid Aditya Rahman [1], Sonki Prasetya [1,2*], Hasvienda M Ridlwan [2]

[1] Mechanical Engineering Department (Renewable Energy Skill Development Program), Politeknik Negeri Jakarta, Jl. SiwabessyA. Siwabessy, UI Campus, Depok, 16425
[2] Center for Conversion, Conservation and Applied Renewable Energies (CARE), Politeknik Negeri Jakarta, Jl. SiwabessyA. Siwabessy, UI Campus, Depok, 16425
* Correspondence: sonki.prasetya@mesin.pnj.ac.id

Abstract: Various PLTS systems have been installed in the Energy Laboratory of Politeknik Negeri Jakarta, ranging from on grid, off grid, and SHS systems, and various sources of PLTH, PLN, and Generator Set (Genset.) However, the problem that occurs there is that the hybrid system in the Lab. Solar System PNJ room cannot be monitored easily and controlled automatically. As a result of these problems, monitoring the performance of hybrid systems and learning in the PNJ Solar Systems Lab cannot be done optimally. The power source in the lab can be combined in a Hybrid PLTS system and generator with a switch method using the ATS switch control system and monitoring for student learning. The purpose of this research will be to analyze the economic value and use of ATS switches for various concepts in saving electricity in a certain period of time using project management analysis so that it can see the feasibility of this project to be implemented or not. The method in this study is to calculate the economic feasibility value, then find the value of Internal Rate of Return (IRR), NPV, Payback Period using Microsoft excel software and analyze project risks. The results obtained in this project are the IRR value> Interest rate, namely 6.51%> 5.75%. The NPV value obtained is Rp. Rp.572,252 with a payback period in year 12. From the results obtained, this project is declared feasible to continue.

Keywords: Control System; Internet of Things (IoT); Solar Hybrid Power Plant

Citation:. Rahman, M., F., A., Prasetya, S., Ridlwan., H., M. (2024). IoT-based Intelligent Monitoring & Control System Planning Using Project Management Method and Business Feasibility Analysis. Recent in Engineering Science and Technology, 2(02), 35–43. Retrieved from https://www.mbi-journals.com/index.php/riestech/article/view/47

Academic Editor: Iwan Susanto

Received: 29 January 2024
Accepted: 29 April 2024
Published: 31 April 2024

Publisher's Note: MBI stays neutral with regard to jurisdictional claims in published maps and institutional affiliations.

1. Introduction

New Renewable Energy (EBT) continues to be intensified to achieve the energy transition target in reducing greenhouse gas (GHG) carbon emissions and preventing global warming. The EBT mix target is 23% in 2025 while in 2022 it was still 12.3% [1]. One of the EBT mix targets is the spread of solar power plants (PLTS). PLTS is one of the EBT power plants that utilizes sunlight to be converted into electrical energy (procedures, villages, and regions n.d.) [2].

In previous research on Goring, Ramba Goring Village, Design of Portable Hybrid Power Plant Plts and Pltmh with Iot-Based Monitoring System conducted research on the design of a hybrid generation system between PLTS and PLTMH [3]. Then the research Analysis of Sensor Selection and Accuracy in Weather Station Design as a Weather Monitoring System for the Jakarta Polytechnic Area [4]. Analyzes the selection of sensors used as monitoring in the plts system. In research of Preliminary Study of Off-grid PLTS Systems as a Mobile SPBKLU Source [5]. Analyzing Calculations to determine the components selected in the Off grid PLTS system using theoretical calculations and comparing with

the PVsyst application in order to reduce the risk of calculation errors. Research conducted by Techno-Economic Analysis of Solar Power Plants (PLTS) at PT Pertamina (Persero) processing unit IV Cilacap [6,7]. The calculation of investment feasibility carried out shows an NPV value of USD 2,128,717.24. PI value = 1.33, IRR value of 18.2%, and DPP value of 11 years. These conditions indicate that the construction of PLTS at PT Pertamina Processing Unit IV Cilacap is feasible. In research on Engineering Analysis and Economic Feasibility in the Design of Hybrid System Solar Power Plants Using analysis methods with PVSyst and RetScreen simulations, this PLTS produces electricity of 1,653.2 kWh / year [8,9]. With an initial investment of Rp 25,186,000, the net present value is Rp 1,210,272 and the pay back period is in the 24th year.

In this research, careful planning is needed so that the Hybrid Solar PV (PLTS) system project runs properly for real implementation [10-12]. The case use the PNJ Solar System Lab location. This research objective is to design the Hybrid Solar PV project with an additional Automatic Transfer Protocol (ATS). The paper compares several concept designs. Project Management which includes an explanation of the management team, stakeholder management, operational and maintenance management, and Business Feasibility Analysis including Financial Analysis, Risk Analysis, SWOT Analysis, and Load Analysis are discussed in this paper. Therefore, a suitable system design can be derived along with an economic analysis of the project on a series of IoT-based intelligent monitoring and control tools in the PNJ Solar System Lab.

2. Materials and Experiment Methods

This research is qualitative research that aims to analyze the economic value and feasibility of this research Hybrid PLTS system project. The focus of this research is to calculate the IRR NPV, Payback Period and Profitability Index values of the project. The system will be validated by clients or users to assess the level of feasibility and ease of use.

The stages of this research include problem identification by observation and discussion, information gathering to find the economic value and feasibility of the project based on the parameters mentioned above using formulas entered Microsoft Excel to facilitate the calculation process.

Before looking for NPV, IRR, Payback period and PI values, it is necessary to analyze the components in the system to see the suitability of specifications and the power generated with the load requirements to be installed through RETScreen software and Global solar atlas to find solar irradiation at the research location.

After finding the economic value, the risk analysis method is carried out with the probability and consequence table by assessing the risk from a scale of 1-5 and then adding mitigation to minimize the risk so that the previous value is reduced.

Formula for finding IRR [13]**:**

To find the NPV value, you can use the following formula:

$$\textbf{NPV} = \sum_{t=1}^{N} \frac{Ci}{(1+i)^t} - Co \quad (1)$$

Ct : Cash Flow per year in period t

Co : Initial Investment Value at Year 0

r : Interest Rate

t : Investment Period

Formula for finding Payback period (PP)

$$\text{PBP} = 0 + \frac{Biaya\ investasi - net\ cash\ flow\ tahun\ ke-1}{cash\ flow\ tahun\ ke-2 - net\ cash\ flow\ tahun\ ke-1}\ x\ 1\ tahun \quad (2)$$

Formula for finding Internal Rate of Return (IRR)

IRR formula:

$$\text{NPV} = 0 = \frac{CF1}{(1+1)\text{^}1} + \frac{CF2}{(1+1)\text{^}2} + \frac{CF3}{(1+1)\text{^}3} + \ldots + \frac{CFn}{(1+1)\text{^}n} - \text{OI} \quad (3)$$

Ket: CF: Cash flow

i : Cost of capital/interest rate sought at discount rate NPV will be zero

n : Lifespan of the investment project

OI : Initial investment

3. Results and Discussion

Final Results

1. Product Design Concept.

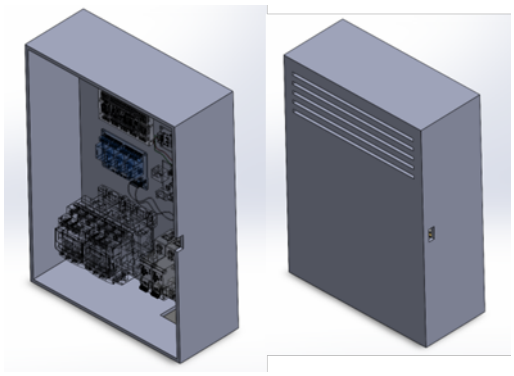

Figure 1. The revised draft of Product Design

In this research, the monitoring and control system will be incorporated into the control panel which is made of two concepts discussed in other subtitles as shown in Figure 1. Of these two concepts, Economic Analysis will discuss the second model which is more favorable according to the survey because with its larger size it will be easier to maintain and replace components later if needed.

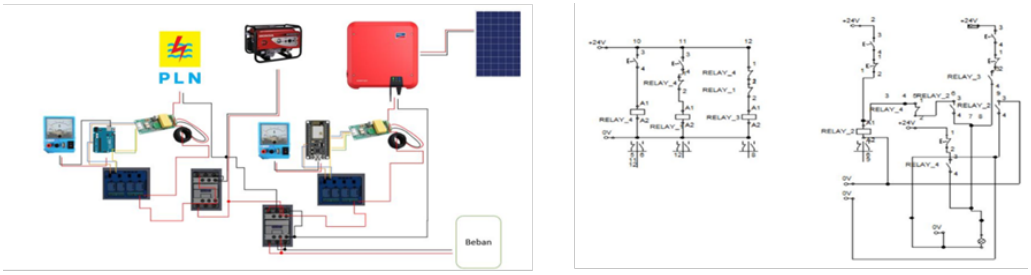

(a) (b)

Figure 2. Hardware circuit of ATS control system shown in figure (a) diagram of ATS control system shown in figure (b).

The hardware circuit details as shown in Figure 2 illustrates the ATS/AMF intelligent control circuit arrangement. In the hardware design for the ATS/AMF control system, it is done by drawing the control and power circuit diagram of the ATS/AMF system. Furthermore, selecting / determining the components to be used such as MCBs, Contactors, Power Supplies, Relays based on the current capacity and performance of the component itself and equipped with monitoring components [14].

Financing project

Table 1. Funding for the Project Concept 1

No	Items	Units	Volume	Prices (Rp)	Total (Rp)
1	Arduino UNO	pcs	2	250,000	500,000
2	Relays	pcs	4	5,000	20,000
3	Contactor	pcs	3	87,000	261,000
4	AC voltage sensor	pcs	2	100,000	200,000
5	modem	pcs	1	125,000	125,000
8	NYM 1.5 power cable	meters	5	25,000	125,000
9	Electric cable NYM 3x2.5	meters	5	25,000	125,000
10	NYM 2025 power cable	meters	5	25,000	125,000
11	Skun (round/Y/feruless) colorful	pcs	30	5,000	150,000
12	Saldar MCB	pcs	2	50,000	100,000
14	Male female jumper cable	pcs	20	1,000	20,000
15	Routers	pcs	1	250,000	250,000
16	anti-lightning splitzen 60cm	pcs	1	145,000	145,000
17	filament	roll	2	210,000	420,000
18	loT module No de MCU ESP32	pcs	1	90,000	90,000
GRAND TOTAL				1,393,000	2,656,000

In this project, the preferred concept is shown in Table 1. The second panel box concept so that the cost is adjusted for the second concept, besides that this research carries 3 Solar Panel (PLTS) system concepts, namely:

In this research, 3 concepts are carried out to be selected conditionally for the client, namely:

Concept 1: Lightning-proof addition + router modem

Concept 2: Lightning-proofing + router addition

Concept 3: Addition of Modem + Router

The cost is adjusted for the concept of 1 solar system as shown in Table 2.

Table 2. Cost of Services

Fixed Service Fees		management fee applied
Design Fees	Rp.300000	Rp 30.000
System programming costs	Rp.250000	Rp. 25,000
Installation costs according to the concept chosen		optional*)
Concept Installation Costs 1	Rp.800.000	Rp.80.000
Concept Installation Cost 2	Rp.600.000	Rp.60.000
Concept Installation Cost 3	Rp. 450.000	Rp.45.000

Then the initial capital price is the cost price + service fee for concept 1 as shown in Table 1. so that the total initial capital for concept 1 is Rp.5,885,000. Then this value will be an input to find the value of NPV, IRR and determine the payback period on this project to determine the feasibility of the project.

Table 3. Total Project Cost

Items	**Prices**	**Notes**
Initial costs before using ATS	Rp.4.721.000	Fixed
Additional RAB Fees Monitoring tools and control	*) concept 1 Rp.2.921.600 *) concept 2 Rp.2.784.100 *) concept 3 Rp.2.613.600	*) Optional
Design service fee + programming	Rp.550.000	Fixed
Installment fee	*) concept 1 Rp.880.000 *) concept 2 Rp.660.000 *) concept 3 Rp. 495.000	*) Optional
Total Cost insstallment equipment	*) concept 1 Rp.4.351.600 *) concept 2 Rp.3.994.100 *) concept 3 Rp.3.658.500	*) Optional

Total investment costs (PLTS+addition tool)	*) concept 1 Rp.9.072.600 *) concept 2 Rp.8.715.100 *) concept 3 Rp.8.379.500	*) Optional

Table 3. above is made with Microsoft Excel so that the capital costs are obtained along with the estimated total operating costs and also the annual power generated from solar panels using the formula 0.8 KWp x 5 x 365 = 1460 Kwh / Year.

Table 4. PV Value of Net Cash Flow

IRR	9.32%
NVP	1,358,644
Pay Back Period	9
RoI	5.8%

Year	Net cash flow	Accumulatif
0	-4,351,600	-4,351,600
1	487,789	-3,863,811
2	487,789	-3,376,022
3	487,789	-2,888,233
4	487,789	-2,400,444
5	487,789	-1,912,655
6	487,789	-1,424,866
7	487,789	-937,077
8	487,789	-449,288
9	487,789	38,501
10	487,789	526,290
11	487,789	1,014,079
12	487,789	1,501,868
13	487,789	1,989,657
14	487,789	2,477,446
15	487,789	2,965,235
16	487,789	3,453,024
17	487,789	3,940,813
18	487,789	4,428,602
19	487,789	4,916,391
20	487,789	5,404,180

IRR	6.51%
NVP	572,252
Pay Back Period	12
RoI	2.4%

Year	Net cash flow	Accumulatif
0	-9,072,600	-9,072,600
1	823,897	-8,248,703
2	823,897	-7,424,806
3	823,897	-6,600,909
4	823,897	-5,777,012
5	823,897	-4,953,115
6	823,897	-4,129,218
7	823,897	-3,305,321
8	823,897	-2,481,424
9	823,897	-1,657,527
10	823,897	-833,630
11	823,897	-9,733
12	823,897	814,164
13	823,897	1,638,061
14	823,897	2,461,958
15	823,897	3,285,855
16	823,897	4,109,752
17	823,897	4,933,649
18	823,897	5,757,546
19	823,897	6,581,443
20	823,897	7,405,340

By using Excel, it is also obtained a comparison of IRR values before and after using the tool of 9.32% and 6.61% The amount of discount rate (i) used to calculate the present value in this study is 5.75% as shown in Figure 4. The determination of this discount rate refers to the Bank Indonesia lending rate as of March 15, 2023. Based on the simulation in Figure 4.3, it is known that the IRR value is> 5.75%, so the project is declared feasible to continue. In the payback period comparison, it can also be seen that the difference in the payback period before and after using ATS where if you don't use ATS. The payback value here means that clients who should pay electricity to PLN every year of Rp.2,108,240 / year with theoretical annual electrical energy production of 1460kWh / year by using PLTS without using ATS with an initial capital of Rp.4,721,600 will return capital in year 9 while if using ATS concept 1 then the return occurs in year 12. In addition, the NPV value of both shows a positive value before and after using the ATS tool, namely Rp.1,358,644 and Rp.572,252. It can be seen that the NVP value after installing the ATS is smaller than before installing the ATS because the initial capital required is greater and the payback period is also longer. In concept 1, although the payback value is longer, concept 1 offers a better safety aspect because there is a lightning rod and smooth data communication in the system so that there is no delay in data using routers and modems so that communication is smoother.

Table 5. Risk Assessment matrix table

		Assessment before measure				*Assessment after measures*			
Risk	Risk description	P	S		Actions (multiple possible)	P	S		Decision
1	Terjadi Kontak dengan sambaran petir	3	5	15	Memasang anti petir dan surge arrester pada sistem PLTS	3	2	6	
2	Shading pada PLTS	4	4	16	survey tempat yang cocok dipasang plts tanpa ada gangguan shading	2	2	4	Diambil
3	Cuaca yang tidak dapat diprediksi berdampak pada produksi daya plts	5	5	25	menambahkan sensor suaca atau berkordinasi dengan bmkg setempat	3	3	9	Diambil
4	Kebakaran Solar Panel	3	5	15	perhatikan saat ada kabel yang putus ataupun rusak, pastikan kebel tersebut diisolasi dengan bena	2	2	4	
5	Kualitas Komponen yang telah dibeli kurang baik	3	3	9	Pengawasan diperlukan selama tahap detail engineering	2	2	4	
6	Pembangkit tidak mencapai kinerja yang diinginkan	3	3	9	Menambahka n peralatan pendukung agar kinerja lebih baik	2	3	6	
7	Delay pada relay yang terlalu lama untuk switch	2	3	6	Mengoptimasikan Sistem baik pada programming maupun perangkat	1	2	2	
8	Keadaan Panel box yang kurang terisolasi dengan baik	3	5	15	tes terlebih dahulu untuk memastikan keadaan terisolasi dengan baik	2	3	6	
9	Muncul Kotoran di permukaan Panel Surya	4	4	16	membersihkan secara rutin/terjadwal	3	3	9	
10	Koneksi Internet untuk monitoring pada IOT bermasalah	4	4	16	Pilih provider yang baik dan pasang routerdan modem	2	2	4	
11	Setelan sensor yang kurang terkalibrasi	3	3	9	mengkalibrasikan sensor dengan alat ukur denan perocbaan beberapa kali hingga mendapat hasil yang akurat	2	2	4	

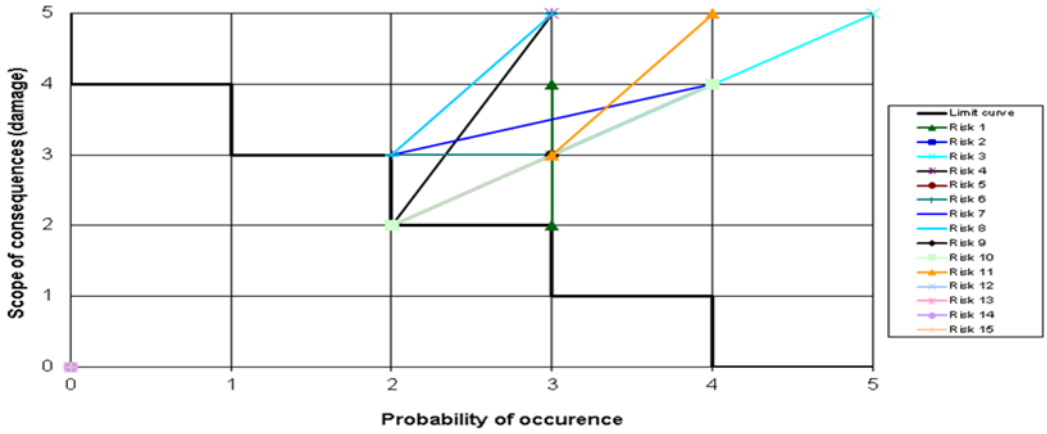

Figure 3. Risk Analysis Chart

Table 5. shows the analysis of risks that could potentially occur along with points on a scale of 1 - 5 for the amount of impact caused and the likelihood of the risk occurring. Then include mitigation actions that may be taken to prevent the risk from occurring.

Figure 3 shows the graph that occurs based on the assessment value given, if the trend position is getting up and to the right, the level of possibility of risk is getting bigger and the impact given is getting bigger. Vice versa, the more to the left and downward, the level of possibility of risk is getting smaller and the impact given is not too large.

In the graph, it can be seen that the biggest level of risk is from weather factors which cannot be predicted and greatly affects the amount of power generated from solar power plants and the benefits that can be taken, followed by uncalibrated sensor settings that can cause false alarms on the system. Then then the delay is too long on the switch where if the switch is too long it can disrupt the ongoing operational conditions if an emergency occurs and followed by other risks.

From the results of the risk analysis for lightning risk and internet connection, special devices are added to minimize these risks which have been grouped in the concepts offered in this study, namely concept 1, concept 2 and concept 3. Lightning-proof installation conditions are optional, especially for areas prone to lightning to improve safety aspects and maintain tool life. And for the addition of modems and routers is also optional where there is also an option to only install a router if you want to use the existing network at the location. If the network is not yet available, you can use a modem and also a router

with a good provider as has been researched in the sub-title "Planning ATS and AMF Control System Design for PLT Hybrid Lab. Solar System PNJ" with the results of the best provider with the fastest upload and download rate is Telkomsel.

4. Conclusions

In the economic analysis in this research carries three concept offers, namely; concept 1, concept 2 and concept 3 for clients whose respective IRR values after installing ATS are compared with the investment value before using ATS with the three different concepts. The value of NVP, IRR is declared feasible to continue with the comparison of the level of electricity cost savings is saving Rp.2,108,240 / year with theoretical annual electrical energy production of 1460 kWh / year. Of the three concepts proposed, if you want a level of safety and comfort of data communication, the concept that should be taken is concept 1 because it includes using anti-lightning and routers and modems with the recommended provider is Telkomsel.

Acknowledgments: The authors would like to thank PT Bakrie Autoparts for the support and opportunity for the availability of facilities to conduct this research.

References

1. Kurbanov, F., Sitenko, D., Yessengeldin, B., Zhumatayeva, B., & Esbergen, R. A. (2020). Organizational and economic mechanisms of energy conservation and energy efficiency man-agement in Kazakhstan. International Journal of Energy Economics and Policy, 10(2), 206-212.
2. Klemeš, J. J., Varbanov, P. S., Ocłoń, P., & Chin, H. H. (2019). Towards efficient and clean process integration: utilisation of renewable resources and energy-saving technologies. Energies, 12(21), 4092.
3. Kamelia, Lia, Khusnul Kharisma, and Afaf Fadhil. 2017. "Economic Planning Analysis of Renewable Hybrid Power Plant (Case Study: Gunung Kidul Regency, Yogyakarta)." TELKA - Telecommunications, Electronics, Computing and Control 3(1): 13-27.
4. Sakti, Bintang Airlangga, Sonki Prasetya, and Isnanda Nuriskasari. "Analysis of Sensor Se-lection and Accuracy in the Design of a Weather Station as a Weather Monitoring System for the Jakarta State Polytechnic Area." Proceedings of the National Seminar on Mechanical Engineering. No. 1. 2022.
5. Permana, Auffanida Fadhila, Sonki Prasetya, and Yuli Mafendro Dedet Eka Saputra. "Pre-liminary Study of Off grid PLTS System as a Mobile SPBKLU Source." Proceedings of the National Seminar on Mechanical Engineering. No. 1. 2022
6. Nugroho, Yusuf Adi. 2016. "Techno-Economic Analysis of Solar Power Plant (PLTS) at PT Pertamina (Persero) Processing Unit IV Cilacap." IEA Clean Coal Center 11(9): Issue 18-4. http://digilib.its.ac.id/public/ITS-Undergraduate-12820-Presentation.pdf.
7. Shahinzadeh, H., NajafAbadi, M. M., Hajahmadi, M., & Paknejad, A. (2013). Technical and Economic Study for Use The Photovoltaic System for Electricity Supply in Isfahan Museum Park. International Journal of Scientific and Technology Research, 2(1).
8. Denis, Denis, Jaka Windarta, Bambang Winardi, and Imam Arifan Nurdani. 2022. "Engi-neering Analysis and Economic Feasibility of Hybrid System Solar Power Plant Design." Infotek-mesin 13(1): 80-86.
9. Riawan, Govinda, I Nyoman Satya Kumara, and W. G. Ariastina. 2022. "Performance and Economic Analysis of 10 KWp Rooftop Solar Power Plant for Household Buildings in Batuan Village, Gianyar." Scientific Magazine of Electrical Technology 21(1): 63.
10. Wicaksono, Chrysti Adi, Imam Supriyadi, M Sidik Boedoyo, and University of Defense. 2020. "Analysis of Costs and Benefits of Using Plts and Pltd (Hybrid) in Meeting the Electricity Needs of Radar Units (Satrad) at the Border (Planning Case Study of Satrad Tni Au Tanjung Sopi, Kab. Morotai Island)." 6: 10-27.

11. Procedure, Standard Operating Procedure, For BUM Desa, and Local Government. "Stand-ard Operating Procedures (SOP) for BUM Desa and Local Government."
12. Ray, Pius Aditya Kurnia, Rony Seto Wibowo, and Feby Agung Pamuji. 2021. "Feasibility Study of 80 KW PLTS Installation in the Electricity System of PT Indonesia Vehicle Terminal." ITS Engineering Journal 10(1).
13. Dai, H., Li, N., Wang, Y., & Zhao, X. (2022, March). The analysis of three main investment criteria: NPV IRR and payback period. In 2022 7th International Conference on Financial Inno-vation and Economic Development (ICFIED 2022) (pp. 185-189). Atlantis Press.
14. Lazuardi, I. A., Farid, I. W., & Priananda, C. W. (2021). Automatic Transfer Switch Dilengkapi Fitur Monitoring Website pada On-Grid Solar Home System. Jurnal Teknik ITS, 10(2), B204-B211.

RiESTech
Recent in Engineering Science and Technology

MBI

Article

Stability Analysis of Feed Gas Based on Pressure using Gas Chromatography at PT Badak NGL

Feby Valentina [1], Muhammad Prasha Risfi Silitonga [1,*], Reza Azhari [2]

[1] Department of Mechanical Engineering, Politeknik Negeri Jakarta, Depok, 16242, Indonesia
[2] PT. Badak NGL, Bontang,, 75324, Indonesia
* Correspondence: m.silitonga@mesin.pnj.ac.id

Abstract: As one of the LNG processing companies in Indonesia, Badak NGL plays an important role in product QA and QC. Laboratory and Environment Control PT Badak NGL obtained ISO 17025 as a testing and calibration laboratory. In clause 7.7 of ISO 17025, stated that each laboratory is required to improve competence, one of which is by holding interlaboratory meetings. Currently, PT Badak NGL is participating in the implementation of the Inter Laboratory Meeting (ILM) in East Kalimantan. In the implementation of the ILM 112th and 113th in 2022, several laboratories provide outlier results in natural gas sample testing. Various factors affect the results of natural gas sample testing, one of them is the sample pressure. This research aims to determine the minimum pressure limit in testing feed gas samples. The test is carried out by designing a series of two cylinders to test the repeatability value. The sampling process is based on GPA 2166 and the measurement of repeatability values is based on GPA 2261. This method is effective for determining the limit of repeatability values as a reference for the minimum sample pressure before being injected into Gas Chromatography.

Keywords: Feed gas; Pressure; Repetability; Gas Chromatography.

Citation:. Valentina, F., Prasha Risfi Silitonga, M., Azhari, R. (2024). Stability Analysis of Feed Gas Based on Pressure using Gas Chromatography at PT Badak NGL. Recent in Engineering Science and Technology, 2(02), 44–54. Retrieved from https://www.mbi-journals.com/index.php/riestech/article/view/52

Academic Editor: Iwan Susanto

Received: 3 Maret 2024
Accepted: 6 April 2024
Published: 31 April 2024

Publisher's Note: MBI stays neutral with regard to jurisdictional claims in published maps and institutional affiliations.

1. Introduction

PT Badak Natural Gas Liquefaction or known as PT Badak NGL is the largest liquefied natural gas processing company in Indonesia and one of the largest LNG refineries in the world. The company is located in Bontang, East Kalimantan, and has 8 process trains (A - H) capable of producing 22.5 Mtpa LNG (million metric tons of LNG per year).

PT Badak NGL is a non-profit company that acts as an operator where natural gas is shipped from producers. Annual report PT Badak NGL 2022 mentioned that Badak LNG obtained feed gas from Muara Badak and supplied by Chevron Indonesia, Pertamina Hulu Sanga-sanga, Pertamina Hulu Mahakam, ENI. Gas from these producers is then piped to a gas processing facility.

As an non-profit company, PT Badak NGL has an important responsibility in reporting the results of testing the compotition of feed gas sent by producers. The result of testing the compotition of the delivered feed gas affects the sale and purchase contract between the producer and the buyer. Therefore, PT Badak NGL must be fully responsible for the implementation of feed gas testing.

PT Badak NGL succeeded in obtaining ISO 17025 accreditation as a testing and calibration laboratory with the scope of accreditation for testing Natural Gas (NG) and Liquefied Natural Gas (LNG). ISO 17025 is an international standard given to laboratories in conducting calibration and testing activities throughout the world. ISO 17025 is able to become a benchmark for laboratories in proving valid test and calibration results that can be widely trusted.

In clause 7.7 ISO 17025, Ensuring the Validity of Results, it is stated that the laboratory must have procedures to monitor the validity of the results. Data generated should be recorded in such a way that trends can be detected and, whenever possible, statistical techniques should be applied to review the results. One of the methods that mentioned in ISO 17025 to ensure the validity of the test results is by holding an interlaboratory meeting. In this case, PT Badak NGL joined the Inter Laboratory Meeting (ILM) in East Kalimantan. The ILM implementation was attended by all natural gas producers, distributors and consumers consisting of 10 laboratories.

ILM is held periodically every 3 months. In the practice of ILM, the series of cylinders used consists of 16 sample cylinders arranged in series. Where two sample cylinders, specifically cylinders no. 1 and 16 are used as verification cylinders, 4 sample cylinders are used as a reserve, and 10 cylinders are distributed to related laboratories. During the implementation of the 112th ILM in June 2022 and the 113th in September, several laboratories provided outlier sample feed gas test results. An outlier result is a condition where the test results of a laboratory are very different from other laboratories according to statistical calculations.

The results of the outlier feed gas sample testing can be caused by several factors, both from the feed gas sampling process, conditioning sample feed gas, and the sample testing process using Gas Chromatography. During the implementation of ILM, all sampling procedures were witnessed by all participants and confirmed according to the GPA 2166 standard concerning Obtaining Natural Gas Samples for Analysis by Gas Chromatography. Furthermore, the homogeneity of the sample cylinder series has also been tested from sample cylinder 1 and sample cylinder 16. Therefore, the cause of the outlier test results can be caused by conditioning the sample cylinder or the testing process with Gas Chromatography.

GPA 2166 has explained the process of conditioning cylinder sample feed gas prior to injection and testing using Gas Chromatography. The document explains that the sample needs to be heated to 11 C above the sample temperature to ensure all components are vaporized before flowing into the detector in Gas Chromatography. The reference document also explains that the flow sample flowing towards the column in Gas Chromatography is set at 3 bubbles per second. Furthermore, the document does not regulate the minimum sample pressure that is injected in Gas Chromatography.

Sample pressure is an important parameter that needs to be controlled in conducting tests using Gas Chromatography. The sample pressure affects the diffusion rate of each component in the column (Scott, Raymond P.W., 2020). As we know that Natural Gas has the most complex components (N_2, CO_2, and alkanes) so that the sample pressure is very influential in giving strength to each component to diffuse to the stationary phase in the Gas Chromatography column.

The complexity of the components possessed by the sample feed gas also affects the stability of the components in repeat testing. Each component gives different test results. These differences are influenced by relative molecular masses, boiling points, intermolecular attractions, and the presence of major and minor components in the sample (G. Gilbert, Seymour, 2021)

This study aims to analyze the stability of sample feed gas based on pressure as alternative strategy to determine the minimum sample pressure limit in feed gas testing and analyze the effect of intercomponent stability in sample feed gas.

This research was conducted at PT Badak NGL. The scope of this research includes the sample feed gas used in the test is limited to only the sample feed gas Train E and the sample cylinder capacity used is 300 cc according to the cylinder in the ILM implementation. The sampling process was carried out based on GPA 2166 with the purging fill and empty method. The sample conditioning process is also based on the document, in which the sample cylinder is heated to a temperature of 11°C above the sample temperature

within 2 hours. The flushing process was carried out for 5 minutes according to the vendor's recommendation and modification of the sample loop on the Gas Chromatography used. The stability value is based on the repeatability value according to GPA 2261.

2. Materials and Experiment Methods

This study will be carried out systematically by comparing the repeatability value of each component according to the limits given in GPA 2261. Initially, two cylinders were assembled in series using identical cylinders. The purpose of this cylinder assembly is to obtain two identical samples as a test material and compare the trends of the two cylinders to ensure the accuracy of the repeatability values.

Before the sample cylinder is assembled, the cylinder is ensured to be clean by washing it and flowing pure water to prevent liquid and impurities from entering the cylinder. The cylinder is also checked for leaks between connections using a liquid leak detector.

After the sample feed gas from Train E is obtained, the sample cylinder is conditioned first by heating the sample cylinder using a belt heater. Figure 1 ilustrate the set up between cylinder sample, belt heater, and Gas Chromatography Agilent 6890N. The sample cylinder is heated to a temperature of 11°C above the sample temperature for 2 hours. When the sample cylinder is heated, the connection between the outlet valve cylinder can be connected to the sample loop on Gas Chromatography.

After the conditioning process is complete, the sample cylinder outlet valve is opened and gas is flowed into the sample loop to ensure that there are no leaks at the connection between the sample cylinder and Gas Chromatography. This is enabled so that sample readings can be representative and no air enters. The flushing process is carried out by flowing the sample for 5 minutes with a constant flow. After that the sample can be tested and the pressure recorded when the flushing process is complete. The sample pressure is varied between 550 psig to 100 psig. Figure 2 ilustrate the overall methodology of experimental.

Figure 1. Experimental Set Up

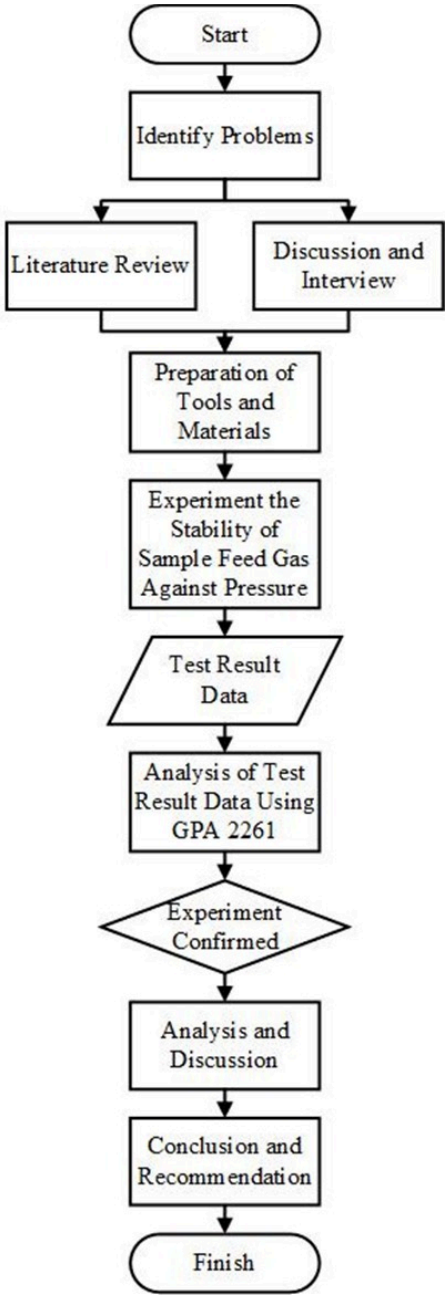

Figure 2. Research Flowchart

Statistical Verification

The verification method used in the test is repeatability in accordance with GPA 2261. There is a formula of statistics for testing repeatability values based on the % mol normalized component which is known from the test results using Gas Chromatography (Table 1). From the results of sample readings in the pressure range, the difference in the largest and highest values can be calculated as well as the average of all readings for each component which is called the x value. The x value can then be substituted into the repeatability formula in Table 1. If the difference value is smaller than the repeatability value, then the sample reading is considered stable and meets the limits, and vice versa. To find out the required minimum sample pressure of feed gas, the value is tested repeatedly from 550 psig to 500 psig, then from 550 psig to 450 psig, and so on until the overall pressure (550 psig to 100 psig).

Table 1. Data Analysis Acceptance Requirements based on GPA 2261

Component	*Range (% mol)*	*Repeatability*
Nitrogen	.02-15	$0.039x^{1/4}$
Methane	50-100	$0.0079x^{1/3}$
Carbon Dioxide	.02-15	$0.0042x^{1/3}$
Ethane	.02-15	$0.0124x^{1/3}$
Propane	.02-15	$0.0084x^{1/8}$
Isobutane	.02-8	$0.01x^{1/5}$
n-Butane	.02-8	$0.0117x^{2/5}$
Isopentane	.02-4	$0.009x^{1/4}$
n-Pentane	.02-4	$0.01x^{1/5}$
Hexane Plus	.02-2	$0.0135x^{1/4}$

3. Results and Discussion

Test Results Data Repeatability Cylinder Sample 1

The repeatability data for the feed gas sample in the first sample cylinder is as follows:

Table 2. Repeatability Sample Feed Gas Cylinder 1

Component (%mol)		N_2	C_1	CO_2	C_2	C_3	i-C_4	n-C_4	i-C_5	n-C_5	C_{6+}
	550	0,054	91,791	3,237	2,152	1,460	0,331	0,400	0,172	0,114	0,289
	500	0,055	91,781	3,240	2,153	1,463	0,332	0,401	0,172	0,112	0,291
	450	0,056	91,768	3,246	2,156	1,466	0,333	0,402	0,172	0,110	0,291
	400	0,055	91,759	3,254	2,151	1,470	0,334	0,402	0,173	0,110	0,293
Pressure	350	0,061	91,716	3,274	2,145	1,482	0,336	0,407	0,174	0,109	0,296
(psig)	300	0,055	91,702	3,282	2,149	1,486	0,337	0,407	0,175	0,109	0,298
	250	0,056	91,677	3,304	2,140	1,496	0,339	0,407	0,176	0,104	0,302
	200	0,066	91,653	3,291	2,173	1,491	0,338	0,409	0,175	0,106	0,299
	150	0,059	91,670	3,299	2,145	1,495	0,340	0,410	0,176	0,106	0,301
	100	0,060	91,640	3,317	2,140	1,504	0,342	0,412	0,177	0,106	0,302
Average normalized mole percent of the component		0,058	91,716	3,274	2,150	1,481	0,336	0,406	0,174	0,109	0,296
***Diff* 1 s/d 10**		0,012	0,151	0,080	0,033	0,044	0,011	0,012	0,005	0,010	0,013
Repeatability		0,019	0,036	0,006	0,016	0,009	0,008	0,008	0,006	0,006	0,010
Result		**PASS**	**NOT PASS**	**NOT PASS**	**NOT PASS**	**NOT PASS**	**NOT PASS**	**NOT PASS**	**PASS**	**NOT PASS**	**NOT PASS**

The formula used in these statistics is mentioned in Table 1. The benefits of the repeatability formula and calculation are used to determine whether in the reading pressure range, the repeatability value of each component still meets the acceptance limits. If there

are components that do not meet these acceptance limits, the pressure reading range can be narrowed and then the repeatability value can be recalculated.

Overall, the repeatability test results of the feed gas sample in the first cylinder show that the nitrogen (N_2) and isopentane (i-C_5) components meet the acceptable repeatability range. Other components in the feed gas do not meet the acceptable repeatability range in the pressure range of 550-100 psig.

Based on Table 2, at a minimum pressure of 500 psig, it shows that all components still meet the repeatability acceptance range in accordance with GPA 2261. Meanwhile at a pressure of 450 psig, the CO_2 component no longer meets the repeatability acceptance range. This continues until the minimum pressure or 100 psig. When the sample reading was carried out at a pressure of 400 psig, component C_3 no longer met the acceptable repeatability range. This is followed by component C_1 at a pressure of 350 psig, components n-C_5 and C_{6+} at a pressure of 250 psig, C_2 and n-C_4 at a pressure of 200 psig, and component i-C_4 at a pressure of 150 psig.

Test Results Data Repeatability Cylinder Sample 2

Repeatability testing on cylinder sample 2 was carried out by the same analyst, namely the author. Repeatability analysis on cylinder sample 2 was carried out with the aim of ensuring that the feed gas sample stability test obtained an accurate minimum pressure value. Testing cylinder sample 2 used identical sampling equipment, the same Gas Chromatography, sample pre-treatment and the same Gas Chromatography running process.

Table 3. Repeatability Sample Feed Gas Cylinder 2

Component (%mol)		N_2	C_1	CO_2	C_2	C_3	i-C_4	n-C_4	i-C_5	n-C_5	C_{6+}
Pressure (psig)	550	0,054	91,764	3,252	2,153	1,468	0,333	0,402	0,173	0,108	0,293
	500	0,055	91,764	3,248	2,156	1,467	0,332	0,402	0,172	0,113	0,291
	450	0,054	91,781	3,240	2,152	1,463	0,332	0,401	0,172	0,114	0,291
	400	0,070	91,730	3,270	2,130	1,482	0,336	0,405	0,174	0,112	0,291
	350	0,058	91,713	3,278	2,144	1,483	0,337	0,407	0,174	0,108	0,296
	300	0,057	91,696	3,286	2,148	1,489	0,338	0,408	0,175	0,107	0,296
	250	0,056	91,644	3,319	2,142	1,503	0,341	0,412	0,177	0,101	0,304
	200	0,061	91,668	3,298	2,143	1,495	0,337	0,416	0,175	0,108	0,299
	150	0,075	91,621	3,320	2,141	1,507	0,342	0,413	0,177	0,100	0,303
	100	0,062	91,621	3,325	2,143	1,509	0,342	0,413	0,177	0,103	0,304
Average normalized mole percent of the component		0,060	91,700	3,284	2,145	1,487	0,337	0,408	0,175	0,107	0,297
Diff 1 s/d 10		0,021	0,160	0,085	0,026	0,046	0,010	0,015	0,005	0,014	0,013
Repeatability		0,019	0,036	0,006	0,016	0,009	0,008	0,008	0,006	0,006	0,010
Result		**NOT PASS**	**NOT PASS**	**NOT PASS**	**NOT PASS**	**NOT PASS**	**NOT PASS**	**NOT PASS**	**PASS**	**NOT PASS**	**NOT PASS**

From the repeatability results of the feed gas cylinder 2 sample, it shows that in the pressure range of 550-100 psig, only the i-C_5 component meets the repeatability acceptance limit of GPA 2261. Based on the data in Table 3, it can be seen that at a pressure of 500 psig

all components in the feed gas meet the repeatability acceptance limit of GPA 2261. At a pressure of 450 psig, the CO_2 component no longer meets the repeatability acceptance limit. In the 400 psig range, components C_1, C_2, and C_3 no longer meet the repeatability acceptance limit. Meanwhile, in the 300 psig range, the n-C_5 component does not meet the repeatability limit, followed by the i-C_4, n-C_4, and C_{6+} components at a pressure of 250 psig, and the N_2 component at a pressure of 150 psig.

Correlation of Repeatability Values for Sample Feed Gas in Cylinder 1 and 2

Overall, the results of the repeatability values for cylinder samples 1 and 2 have the same sample stability values. Starting from a pressure of 450 psig, the two samples do not meet the repeatability acceptance value according to GPA 2261 for the CO_2 component. Then, gradually other components do not meet the repeatability value range.

Effect of Pressure on Repeatability Values

Gas chromatography is a chromatographic technique that uses the principle of separating mixtures based on differences in migration speeds of the constituent components (Maráková, K., Opetová, M., & Tomašovský, R., 2023). In gas chromatography, pressure is an important parameter that can influence the retention time and peak shape of the analyte. In gas applications, fluctuations in gas pressure can affect the velocity of particles in the gas. According to the kinetic theory of gases, pressure is influenced by static pulsations between molecules (Handayani, H., 2020). The pressure is caused by collisions between molecules moving at different speeds. In this case, when the pressure in the sample is measured to be large, this indicates that the collisions produced by the particles in it are also large.

Fick's law of diffusion (Flick's Law) describes the relationship between diffusion and other factors. Flick's Law in equation 5 states that the rate of movement of molecules through a material is proportional to the concentration gradient (concentration difference) between the two ends of the material and is inversely proportional to the thickness of the membrane (Won, Y. Y., & Ramkrishna, D., 2019). So according to this law, greater pressure (difference in pressure concentration) will have an increasing effect on the diffusion rate. This is because the greater the pressure difference, the greater the collision force between particles, so that the rate of particle movement will be greater and the rate of diffusion will be greater.

Based on repeatability data on cylinder samples 1 and 2, the lower the pressure, the more the sample composition reading is out of the repeatability acceptable range. The greater the pressure difference between the column cylinder sample and the Gas Chromatography column, the greater the rate of diffusion that occurs in the column. The greater the diffusion rate, the greater the particle movement speed.

Increasing the diffusion rate affects changes in the response of the Gas Chromatography detector. Increasing the diffusion rate will affect the distribution of particles in the detector where the particles will move faster so that the resulting retention time will be smaller. A substance with a faster diffusion rate will reach the detector more quickly in a given time than a substance with a slower diffusion rate.

Low particle movement speed as a result of a decrease in sample pressure can affect the reading time of components in the detector. The lower the pressure, the lower the particle speed. This results in the retention time read by Gas Chromatography being longer. Peak retention time is one of the components that influences quantitative and qualitative analysis in Gas Chromatography. When there is a change in retention time that exceeds the normal retention time, this results in errors in the reading and calculation of the sample area. As a result, the calculation of the read sample composition is not representative and has a repeatability value outside the permitted range.

Qualitative analysis is generally reflected in the chromatographic peak retention time, which requires peak height and peak area parameters. Generally, the width of the chromatographic peak will be influenced by variable retention times. The longer the retention time, indicates that the particles move more slowly and spread out in the column.

This will have the effect that the width of the chromatogram peaks formed will be wider. The relationship between retention time and baseline peak width of the chromatogram, namely when the retention time is short the peak width is small, has a high peak, and the peak area is relatively small. Meanwhile, the retention time is long, has a large chromatographic peak width, low peak height, and relatively large peak area.

The relationship between retention time and peak width of the resulting chromatogram influences the theoretical plate number (N). In accordance with the theoretical plate formula in equation 3, when a small pressure results in a larger retention time and a larger baseline peak chromatogram width, this will result in a smaller number of theoretical plates. On the other hand, when the pressure is large, it results in a faster retention time with a smaller baseline peak chromatogram width, resulting in a larger number of theoretical plates.

Gas Chromatography columns that have a large number of theoretical plates are more efficient at separating samples compared to columns with a low number of theoretical plates. The concept of plate count as a measure of efficiency is based on separation by distillation. The ability to separate by distillation is reflected in the number of plates, where each plate has a different equilibrium. The greater the number of plates, the better the separation potential.

In accordance with the theory that has been described, the effect of decreasing pressure has a related effect between one parameter and another in reading samples using Gas Chromatography. When the pressure is low (the pressure gradient is small), it can result in a smaller number of theoretical plates, thus indicating a worse component separation efficiency. As a result, the reading of the sample composition in chromatography will experience changes and cause the repeatability value to not meet the acceptance range according to GPA 2261.

Intercomponent Stability in Cylinder 1 and 2

Based on the results of repeatability calculations for cylinder samples 1 and 2, the results showed that the carbon dioxide (CO_2) component was the first component to experience reading instability at a pressure of 450 psig. Continuously, reading the sample gives results beyond the acceptable limit of repeatability up to the smallest pressure (100 psig). Meanwhile, other components gradually experience repeatability instability up to a pressure of 100 psig.

The influence of component stability on the composition identification process using Gas Chromatography is closely related to the diffusion process that occurs therein. Graham's law states that the rate of diffusion of a gas is inversely proportional to the root mass of its particles. In other words, at the same temperature and pressure, the speed of gas diffusion is inversely proportional to the root of its density. In the diffusion process, the smaller the particle size, the faster the particle will move, so the diffusion speed is higher.

Apart from that, the diffusion process is also influenced by intermolecular attractive forces. CO_2 compounds and alkane compounds are both nonpolar covalent compounds. As a result, both compounds have zero dipole moment. However, according to organic chemistry theory, if two nonpolar compounds are close together, an attractive force occurs between the negatively charged electrons of one molecule and the partial positive charge in the other molecule.

In the sample feed gas component, CO_2 is the first component to experience reading instability. This is influenced by the type of compound in each component. CO_2 is an inorganic compound, while the hydrocarbon alkane compound which is the major component is an organic compound. In accordance with basic theory, Gas Chromatography is generally used to separate volatile compounds. If the analysis target is not volatile, it will generally be derivatized (reacted) to become a volatile compound. Carbon dioxide (CO_2) is a non-volatile gas and is not considered a volatile organic compound. Therefore, even

though CO_2 has a low boiling point, namely -78.46°C, this compound is difficult to separate and evaporate by the Gas Chromatography component.

Apart from the volatile nature of the CO_2 compound, the influence of the chain shape of the CO_2 compound also has an influence on the rate of diffusion and the London force that occurs. The CO_2 compound has the same molecular mass as the C_3 compound. However, compound C_3 has a much longer and straighter compound structure. As a result, the attractive force that occurs in the C_3 compound is much greater than the attractive force in the CO_2 compound. This attractive force influences the rate of diffusion that occurs, the greater the attractive force, the slower the resulting diffusion rate. Therefore, the resulting retention time when the pulling force is large is much shorter, so that the deviation in the peak width of the chromatogram will be smaller and the reading will be much more stable.

Although in Graham's theory it is stated that components that have a lighter molecular weight have a faster diffusion rate, this is also influenced by the major factors of composition and shape of the compound chain. In the feed gas sample, the component that has the smallest molecular mass is the C_1 component. However, this component is a major component where 91% of the feed gas component is dominated by methane. As a result, the changing reading value does not have such a significant effect compared to other components that have a lighter molecular weight than C_1. In this case, components C_2 and C_3 are the components that are more unstable than component C_1. Small value changes in components C_2 and C_3 have very influential results on the repeatability range, because these components are minor components where the range for C_2 and C_3 is 1-5%. In addition, the n-pentane component also shows unstable values compared to the values for the n-butane and iso-butane components. This is because the n-pentane component is much smaller than the n-butane and iso-butane components in the overall feed gas component.

4. Conclusions

The repeatability calculation process in accordance with GPA 2261 has its own limits for each component, where the variable used in the calculation is the x value which represents the normalized mol % component. Based on the results of research conducted, the minimum pressure limit for testing feed gas is 450 psig. At this pressure, all components meet the repeatability acceptance limit, where the difference between the largest and smallest reading composition values is smaller than the calculated repeatability value. At this point, the difference value obtained in the composition of C_1 in cylinder 1 was 0.006 and the value of C_1 in cylinder 2 was 0.001, which was smaller than the calculated repeatability value of 0.019. therefore, the component meets the acceptance limits and so do the other components. Pressure has a significant influence on the repeatability results of component readings. Based on Ficks' Law, the greater the pressure gradient, the greater the influence on the acceleration of the rate of diffusion that occurs. As a result, the particles will move faster towards the detector and the peaks formed will be taller and slimmer. The peak shape and retention time influence the calculation of the number of theoretical plates used as an indicator of separation efficiency in the column. The slimmer and faster the retention time, the greater the number of theoretical plates. Therefore, the separation process that occurs is more effective so that the components have good repeatability values.

Acknowledgments: It would not have to possible to finish this paper without the assistance of the working group responsible for Laboratory and Environtmental Control PT Badak NGL and also Politeknik Negeri Jakarta.

References

1. PT Badak NGL. (2018). Welcoming the Bright Future by Increasing Excellence Welcoming the Bright Future by Increasing Excellence 2018 Annual Report Annual Report.
2. PT Badak NGL. (2019). Company Profile PT Badak NGL. PT Badak NGL.
3. PT Badak NGL. (2020). Maintaining Excellence amidst Challenges Maintaining Excellence in an Age of Challenges.
4. Badak LNG Laboratory. (2022a). 112th Natural gas analysis correlation test report between Oil & Gas Companies in East Kalimantan.
5. BadaK LNG laboratory. (2022b). 113th natural gas analysis correlation test report between Oil & Gas Companies in East Kalimantan.
6. Faridah, D. N. et al. (2018). Implementation of SNI ISO/IEC 17025:2017 General Requirements for Competency of Testing Laboratories and Calibration Laboratories. In the Implementation of SNI ISO/IEC 17025:2017 General Requirements for Competency of Testing Laboratories and Calibration Laboratories (ISBN Number: 978-602-9394-22-1). National Standardization Agency.
7. Zaidi Oktari, M., S. R. P., M. F. (2023). Improving the quality of the ibbn test and calibration laboratory through proficiency tests / comparison tests according to the requirements of iso/iec 17025:2017. Journal of quality assurance of the state hindu university I Gusti bagus sugriwa denpasar quality assurance institution, Volume 9 Number 1 (ISSN: 2407-912X (Print ISSN: 2548-3110 (Online).
8. Handayani, H. (2020). Preparation of Virtual Laboratory Based Learning Tools on Gas Kinetic Theory Material (Doctoral dissertation, UIN Ar-Raniry Banda Aceh).
9. Rohman, A. (2020). Pharmaceutical Analysis by Liquid Chromatography. Gajah Mada University Press.
10. Littlewood, A. B. (2013). Gas Chromatography: Principles, Techniques, and Applications (Second Edition).
11. Poole, C. (2022). Gas Chromatography (Second Edition).
12. Leba, M. A. U. (2017). Textbook: Extraction and Real Chromatography (First Printing). Deepublish.
13. GPA 2166-05 Obtaining Natural Gas. (n.d.).
14. Hierdawati, T., Dani, R. (2022). Analysis of natural gas sales volume through pipelines by customer type (mmscf) in indonesia, 2010-2020. Journal of Intellectual Treasures, 6(3). https://doi.org/10.37250/khazanah.v6i3.174
15. Scott, R.P.W. (2020). Techniques and Practice of Chromatography (1st ed.). CRC Press. https://doi.org/10.1201/9780367811914
16. Lestari, F. (2013). Chemical Hazards: Sampling and Measurement of Chemical Contaminants in the Air (MOLD 2013).
17. Gilbert, S. G. (2021). Inverse gas chromatography. In Advances in Chromatography (pp. 199-228). CRC Press.
18. Producers Association, G. GPA 2261: Analysis of Natural Gas and Similar Gaseous Mixtures by Gas Chromatography.
19. Maráková, K., Opetová, M., Tomašovský, R. (2023). Capillary electrophoresis-mass spectrometry for intact protein analysis: Pharmaceutical and biomedical applications (2018–March 2023). Journal of Separation Science, 46(15), 2300244.
20. Scott, R. P. W. (2017). Introduction to Analytical Gas Chromatography, Revised and Expanded (Second Edition).
21. Hindayani, A., Hamim, N. (2022). Accuracy and precision of secondary method of conductivity measurement using jones type e cells for monitoring drinking water quality. IJCA (Indonesian Journal of Chemical Analysis), 5(1), 41–51. https://doi.org/10.20885/ijca.vol5.iss1.art5
22. Won, Y. Y., Ramkrishna, D. (2019). Revised formulation of Fick's, Fourier's, and Newton's laws for spatially varying linear transport coefficients. ACS omega, 4(6), 11215-11222.

23. Faramawy, S., Zaki, T., Sakr, A. A. E. (2016). Natural gas origin, composition, and processing: A review. In Journal of Natural Gas Science and Engineering (Vol. 34, pp. 34–54). Elsevier B.V. https://doi.org/10.1016/j.jngse.2016.06.030
24. Anggraini, V. (2018). Steroid Isolate Toxicity Test from Column Chromatography Results with Variations in Eluent Gradients of the Ethyl Acetate Fraction of The Macroalgae Eucheuma Cot-Tonii. [24]
25. Gritti, F. (2013). The van deemter equation assumptions, limits, and adaptation to modern HPLC. Journal of Chromatography A. [25]
26. Adikharisma, R. (2014). Performance Analysis of the Co_2 Removal Process in the Absorber Column in the Ammoniac Factory Unit 1 Pt. Gresik petrochemistry. Sepuluh November Institute of Technology. [26]

RiESTech
Recent in Engineering Science and Technology

MBI

Article

Study on Engine Learning Experiencing Low Power On Cummins QSL 9.3L Engine

Raihan Trinanda Agsya [1], Rahman Filzi [1], Rahmat Noval [1], Hong Yue [2]

[1] Mechanical Engineering, Politeknik Negeri Jakarta, Jl. Prof. G. A. Siwabessy, Kampus UI, Depok, 16425, Indonesia
[2] Study Program of Applied Technology of Contruction Marchinery, Departement School of Automotive Engineering, Liuzhou Vocational and Technical College, Shewan Rd, Yu Feng Qu, Liu Zhou Shi, Guang Xi Zhuang Zu Zi Zhi Qu, China, 545005
* Correspondence: raihantrinandaagsya@gmail.com

Abstract: The Cummins QSL 9.3L diesel engine is a production engine from CLG or Cummins Liugong. This type of engine is typically used in heavy equipment such as Wheel Loaders. A diesel engine is an internal combustion engine where the combustion process occurs inside the engine itself, and pure air is compressed within the combustion chamber, resulting in high air pressure. It operates in four strokes. This engine experienced low power, causing it to malfunction, which led to abnormal operation. Various checks were conducted, including inspection of diesel fuel, fuel tank inspection, engine oil level check, visual inspection of the air cleaner, water separator check, Fuel Feed Pump check, and Clearance Valve Lash check. The problem identified was the mismatch of Valve Lash clearance in the engine, resulting in low power. The repair step involved adjusting the Valve lash using a Feeler Gauge. The purpose of this research is to provide an explanation of troubleshooting and to perform repairs on engines experiencing low power.

Keywords: Engine Low Power; Valve Lash; Wheel Loader; Troubleshooting

Citation:. Agsya, R. T., Filzi, R., Noval, R., Yue, H. (2024). Study on Engine Learning Experiencing Low Power On Cummins QSL 9.3L Engine. Recent in Engineering Science and Technology, 2(02), 55–64. Retrieved from https://www.mbi-journals.com/index.php/riestech/article/view/55

Academic Editor: Iwan Susanto

Received: 24 April 2024
Accepted: 30 April 2024
Published: 30 April 2024

Publisher's Note: MBI stays neutral with regard to jurisdictional claims in published maps and institutional affiliations.

1. Introduction

A wheel loader is a tractor with rubber tires equipped with a bucket. Wheel loaders are versatile tractors widely used in construction work, especially related to infrastructure construction[1]. Diesel engines in heavy equipment and transportation industries worldwide, including the Cummins QSL 9.3L engine, are known for their power, performance, and outstanding durability. This engine is utilized in various applications, ranging from commercial trucks to construction equipment and industrial machinery.

Engines play a significant role in heavy equipment units as the primary driving force. Various types and brands of engines are used for the main propulsion of heavy equipment units, necessitating a thorough understanding of each type of engine used

The Cummins QSL 9.3L diesel engine is a product of CLG (Cummins Liugong). This type of engine is typically used in wheel loader-type heavy equipment. With its capacity tailored to its needs, this engine is very popular in the heavy equipment industry.

A diesel engine is an internal combustion engine where the combustion process occurs inside the engine itself (internal combustion engine), and pure air is compressed inside the combustion chamber (cylinder), resulting in high air pressure. The diesel engine operates in four strokes[2].

The principle of a diesel engine's operation is to convert chemical energy into mechanical energy. Chemical energy is obtained through a chemical reaction, namely the combustion of fuel (diesel) and oxidizer (air) inside the cylinder (combustion chamber)[3]. A diesel engine is a piston combustion engine whose ignition process does not involve electric spark ignition. Only air enters the cylinder during the intake stroke[4].

Low power engine is a condition where the power generated by the engine decreases, resulting in the unit's inability to operate at its maximum capacity[5]. One of the causes is low power. When the engine experiences low power, it can lead to various problems, including decreased performance, increased fuel consumption, and even further damage to engine components.

Troubleshooting is a type of problem-solving for systems experiencing issues. The purpose of this research is to identify the troubleshooting experienced by the Cummins QSL 9.3L Engine operating as a Learning Engine or Prototype Engine and to determine what damages occur in engines experiencing Low Power and to repair the engine accordingly

2. Materials and Experiment Methods

The author begins by defining the topic, which involves identifying issues with the Cummins QSL 9.3L Engine. The problem statement in this case is to analyze the root causes of Low Power in the Cummins QSL 9.3L Engine owned by LVTC Campus. Based on data collected from field observations, several issues are identified, such as inadequate maintenance of the engine and susceptibility to contamination. Therefore, the author aims to analyze the Cummins QSL 9.3L Engine using the Root Cause Analysis (RCA) method. To analyze the factors causing the engine to experience Low Power, the author conducts a literature review to find relevant sources in books/journals related to Low Power Engines. From the analysis, the author identifies the factors causing the Low Power in the engine and suggests preventive measures through regular maintenance. Subsequently, testing steps are conducted, including Fuel Tank Inspection, Oil Level Inspection, Visual Inspection of the Air Cleaner, Fuel Filter Water Separator Inspection, Fuel Feed Pump Inspection, and Clearance Valve Lash Inspection on the engine[6].

In problem-solving method, Root Cause Analysis (RCA) is employed. According to Dogget (2005), there are several RCA tools available, including Fault Tree Analysis, Event Tree Analysis, Systematic Cause and Analysis Tool (SCAT), and Fishbone Diagram (Satryawan, 2016). In this research, the author uses Fishbone Diagram and Root Cause Table to analyze the causes of the QSL 9.3 engine experiencing Low Power. The Fishbone Diagram method aims to identify the root causes and determine the subsequent effects. This method helps to visualize the problem more comprehensively, enabling the author to identify a broader scope of causes and effects accurately. The author then details the factors causing the problem, leading to the discovery of the root cause using the Root Cause Table.

The initial step involves checking the condition of the engine oil. Ensure the engine is turned off and the unit is positioned on a level surface. Then, visually inspect the engine oil by reading the dipstick level. The result shows that the engine oil level is between the upper and lower lines or that the volume of engine oil is within normal range.

Problem Solving Methods

Dogget (2005) mentions several Root Cause Analysis (RCA) tools that can be used to identify the root causes of problems[7]. Among them are Fault Tree Analysis, Event Tree Analysis, Systematic Cause and Analysis Tool (SCAT), and Fishbone Diagram[8]

Tools and Materials

Before conducting this research, pay attention to the key points in conducting field research, which require the use of personal protective equipment and work equipment as follows: Gloves, Safety Shoes, Coveralls, Safety Glasses, Tools, feeler gaug

Flowchart

For Cummins diesel engines experiencing low power, we implement several methods in data and information collection including observation, interviews, literature review using the 8-step Troubleshooting, troubleshooting, and repairs. The research steps mentioned above can be seen through the flowchart.

Table 1. Engine Specification Cummins QSL 9.3L

Model	QSL 9.3L
Type	In line, 4 stroke, Direct Injection
Intake	TCAC
Displacement	9.3L
Rated Power	162-180 KW (220-245 HP)
Rated Speed	2200 RPM
Peak Torque	1187N.m
Emission	National III/Tire IIIA
Wet Weight	770 KG
Size	1128*805*1085 mm
Application	Wheel Loader
Firing Order	1-5-3-6-2-4

Here are the specifications of the Cummins QSL 9.3L Engine, a diesel engine used for wheel loader units [9]. The standard specifications are as follows:

Re-measurement of valve clearance using a feeler gauge, which is used to adjust valves. With Torque Value [10].

3. Results and Discussion

The engine lacks power during operation, leading to inadequate engine performance, difficulty in starting, and excessive fuel consumption. After conducting inspections using various methods including observation, interviews, literature review, troubleshooting, and repairs, there is a possibility of issues causing the engine to experience low power.

"Implementation and testing of the system are stages in applying a designed and built system. Here is the display of the implementation and testing of the Expert System diagnosing Engine Low Power in Caterpillar heavy equipment at PT. Trakindo Utama."[11]

Possible Causes of Engine Low Power:[12]

a. Poor quality diesel fuel

b. Insufficient oil

c. Dirty fuel tank

d. Clogged air cleaner

e. Clogged water separator

f. Fuel pipe leaks

g. Clogged fuel feed pump

h. Clogged line pump

i. Incorrect valve clearance

After identifying the possible causes of engine low power, the next step is to inspect each component that could be contributing to the issue.

Component Inspection Steps:

a. Fuel tank inspection

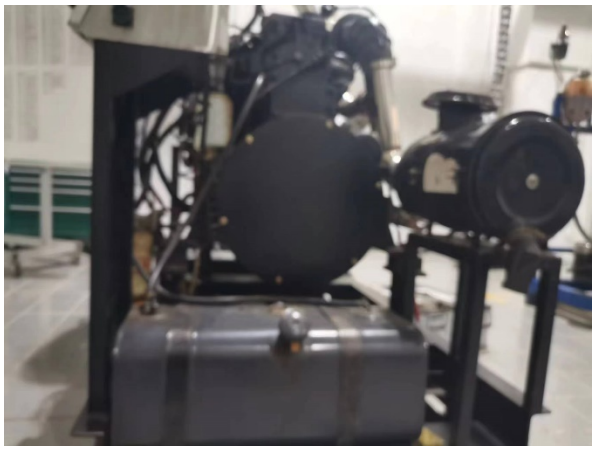

Figure 1. Fuel tank

As a fuel storage place, the fuel tank plays a crucial role in the fuel system. The visual inspection of the fuel tank did not reveal any leaks or fuel tank cap leakage, which could lead to fuel contamination, such as water contamination.

b. Engine oil level check

Figure 2. Oil Level

Checking the oil level of the QSL 9.3L diesel engine. The diesel oil level check showed no shortages, and the oil content appeared to be in good condition and suitable for use.

c. Visual inspection of the air cleaner

Figure 3. Air Filter

The visual inspection of the air filter element showed no dust or dirt buildup on the air filter, and after inspection, the air filter element was reinstalled into the engine.

d. Water separator check

Figure 4. Water separator

Checking the water separator by draining the fuel mixed with water or contaminated with water by opening the drain plug on the water separator. This check revealed water in the water separator, and draining the water separator removed contaminants from the diesel fuel.

e. Fuel Feed Pump Check

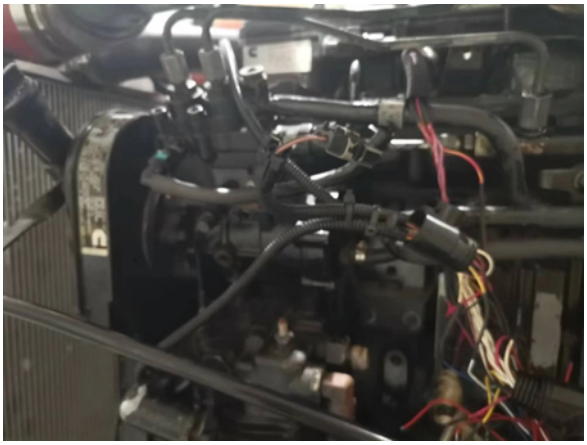

Figure 5. Fuel feed pump

Its function is:

Supplying fuel to the fuel pump at low pressure, ranging from 1.2 - 2.6 kg/cm2. Together with the priming pump, it supplies fuel to the system when the engine is in an air-intruded condition (engine hunting = air entering the fuel system)[13].

Checking the fuel feed pump revealed no fuel pump leaks, and the pressure measurement on the fuel pump was normal. Fuel in the injection pump chamber must always be sufficient, requiring fuel to be delivered to the injection pump under pressure because the pump element cannot deliver enough fuel at high speeds. Therefore, the filling pressure is adjusted to 1.8 – 2.2 kg/cm2 (25.6 – 3 psi) by the piston spring[14].

f. Valve Clearance Check

Figure 6. Valve Clearance

The next step after conducting all visual and specified tool inspections, from the easiest to the most difficult, was identifying the root cause of the engine experiencing low power, which was the mismatch of valve lash clearance on the Cummins QSL 9.3L engine, leading to decreased engine performance.

The next step is to rotate the crankshaft clockwise until cylinder number 1 is in the compression position, where the piston is at Top Dead Center. In this position, you can perform the initial clearance check as follows[15].

Table 2. Checking Top 1 Valve Clearance

Top 1	Result Valve Clearance check	
	Intake	Exhaust
1	O,25 mm	0,50 mm
2	0,28 mm	-
3	-	0,40 mm
4	0,25 mm	-
5	-	0,50
6	-	-

From the Top 1 inspection, it was found that the valve clearance did not comply with the specifications of the QSL 9.3L diesel engine, specifically for the intake cylinder 2 and the exhaust cylinder 3. This deviation from the standard valve lash is a potential cause of the engine experiencing low power.

Table 3. Checking Top 6 Valve Clearance

Top 1	Result Valve Clearance Check	
	Intake	Exhaust
1	-	-
2	-	0,55 mm
3	0,25 mm	
4		0,51 mm
5	0.30 mm	
6	0,35 mm	0,40 mm

From the table above, after measuring the valve lash, discrepancies were found in the standard valve lash for intake cylinders 5 and 6, and for exhaust cylinder 2 and 6. Therefore, based on this measurement, there is a potential cause for the QDL 9.3L engine to experience Low Power

The standard specifications for the QSL 9.3L Engine are as follows:

Table 4. Standard Valve Lash Clearance Specifications

Intake	0,254 mm (0.010 in)
Exhaust	0.508 mm (0.020 in)

Repair Process:

The repair process involves readjusting the valve lash according to the specified reference, with the valve lash readjustment process performed in accordance with the working procedure. After completing all the inspection sequences, the issue of Low Power Engine due to non-compliant Valve clearance was identified. The steps for remeasuring are as follows:

Ensure the engine is in the top dead center (TDC) position to determine the position of cylinder number 1 and then

Figure 7. Determining Top 1 Cylinder

Determining the valves that can be adjusted at the top compression of cylinder 1 can be done by referring to the diagram/table of the cylinder working process or by physically moving the rocker arms. If the rocker arm moves freely, it indicates that the corresponding cylinder can be adjusted.[16][17].

Figure 8. Adjust Valve Lash

Figure 8 above shows the process of readjusting the Valve Lash clearance on the Cummins QSL 9.3L Engine using a feeler gauge, which is used to measure the gap between the rocker arm and the valve.

4. Conclusions

After conducting the inspection and repair procedures on the Cummins QSL 9.3L Engine, the author made observations, inspections, and repairs on the engine experiencing low power due to the mismatch of Valve Lash clearance. The conclusion drawn is as follows:

The Cummins QSL 9.3L Engine experienced low power due to insufficient maintenance, resulting in low power. The cause of the low power engine is the mismatch of Valve Lash Clearance in the engine. The repair efforts undertaken on the low power QSL 9.3L Engine involved various inspections from easy to hard, which were carried out until the problem was identified. Subsequently, adjustments were made to the valve lash according to the existing specifications.

Acknowledgments: The author would like Thank you to Liuzhou Vocational & Technical College for providing the practice facilities and conducting research during my time there as part of the Independent Campus Program.

References

1. D. Moduln D. Q. Y. You, "Shift strategy of a new continuously variable transmission based wheel loader," Mechanism and Machine Theory," vol. 130, pp. 313–329, 2018.
2. A. K. Samlawi, "Teori Dasar Motor Diesel," J. Tek. Mesin, p. 126, 2012.
3. P. Yulianto, "Pengaruh Variasi Putaran Mesin terhadap Daya pada Engine Cummins KTTA 38 C," J. Ilm. Pendidik. Fis. Al-Biruni, vol. 5, no. 1, pp. 23–32, 2016, doi: 10.24042/jpi-falbiruni.v5i1.102.
4. D. Y. Widya, "Motor Diesel Pada Mobil".
5. H. Fathuroyan, P. Studi, T. Mesin, F. Teknik, and U. M. Surakarta, "DIESEL ENGINE LOW POWER PADA UNIT WHEEL LOADER DOOSAN SD 200 N," 2022.
6. Haryanto Dwi, "Jasa Teknisi Komputer," p. 100, 2001.
7. R. F. Fauzi and D. Junaedi, "Analisa Penyebab Low Power pada Travel Motor Excavator 922E Unit Liugong," pp. 1791–1800, 2022.
8. C. A. SATRYAWAN, "ANALISA PENYEBAB KECELAKAAN KERJA DENGAN METODE PIRAMIDA KECELAKAAN DAN ROOT CAUSE ANALYSIS PADA PROSES PRODUKSI PUPUK ZA DI PT. PETROKIMIA GRESIK," 2016, [Online]. Available: http://eprints.umg.ac.id/cgi/oai2
9. K. B. Syariah and G. Ilmu, "ANALISIS AKAR MASALAH (ROOT CAUSE ANALYSIS) KECURANGAN AKADEMIK PADA SAAT UJIAN," no. september 2016, pp. 1–6.
10. "wheel-loader-870h.pdf."
11. G. S. Winata, "Sistem Pakar Mendiagnosa Engine Low Power Pada Alat Berat Caterpillar di PT . Trakindo Utama Dengan Menggunakan Metode Teorema Bayes," no. x, pp. 1–15.
12. T. M. Trakindo, "'Rental Store,' ," pp. 1–2.
13. Q. R. Guide, "Motorhome Maintenance and Operation Motorhome Maintenance and Operation," pp. 8–9, 1997.
14. I. L. Centre, "Basic Course Diesel Engine," 2016.
15. Anonim, "Technical Guide Toyota Diesel. Jakarta : PT. Toyota Astra Motor.," 1995.
16. P. Dasar, "Di esel en gi n e," 2005
17. M. Diklat, B. Kompetensi, S. S. Motor, and K. Modul, "No Title".

PT. Mencerdaskan Bangsa Indonesia

PT MENCERDASKAN BANGSA INDONESIA (MBI), 4th Floor Gedung STC Senayan Room 31-34, Jl. Asia Afrika Pintu IX, Jakarta 10270, Indonesia.